UCSF

UC San Francisco Previously Published Works

Title

A Calmodulin C-Lobe Ca2+-Dependent Switch Governs Kv7 Channel Function

Permalink

https://escholarship.org/uc/item/0dr1g0tf

Journal

Neuron, 97(4)

ISSN

0896-6273

Authors

Chang, Aram

Abderemane-Ali, Fayal

Hura, Greg L

et al.

Publication Date

2018-02-01

DOI

10.1016/j.neuron.2018.01.035

Peer reviewed

eScholarship.org Powered by the California Digital Library
University of California

Article

Neuron

A Calmodulin C-Lobe Ca^{2+}-Dependent Switch Governs Kv7 Channel Function

Graphical Abstract

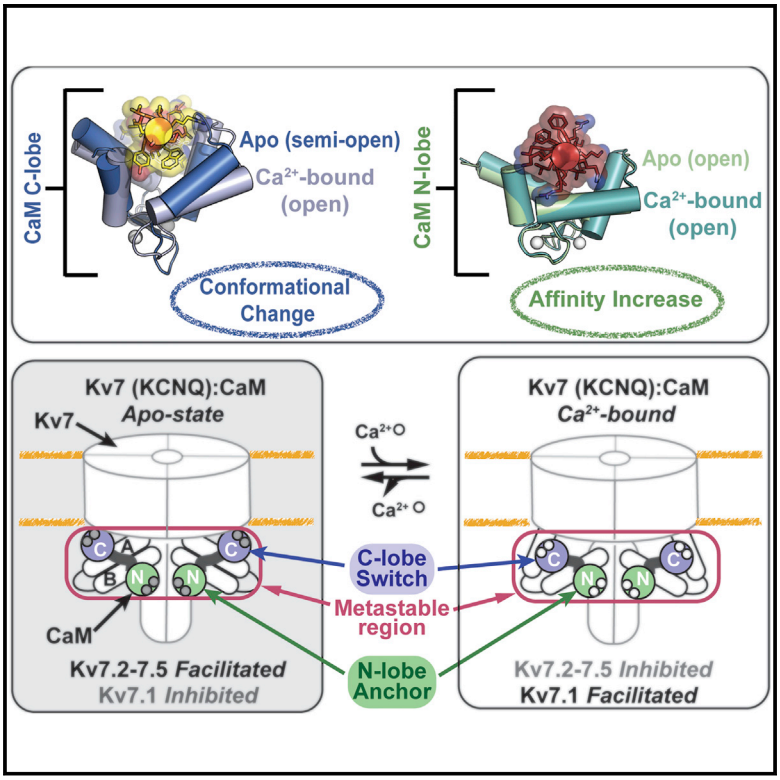

Highlights

- Apo/calmodulin (CaM) forms a clamp around membrane proximal Kv7 AB domains
- Ca^{2+} activates a CaM C-lobe switch, releases the clamp, and anchors CaM N-lobe
- Apo/CaM clamp release inhibits neuronal Kv7.2–Kv7.5 but facilitates Kv7.1 function
- Kv7 pore and coiled coil frame the Kv7 membrane proximal domain metastable switch

Authors

Aram Chang, Fayal Abderemane-Ali, Greg L. Hura, Nathan D. Rossen, Rachel E. Gate, Daniel L. Minor, Jr.

Correspondence

daniel.minor@ucsf.edu

In Brief

Chang and Abderemane-Ali et al. define a unified framework for calmodulin (CaM) control of Kv7 (KCNQ) channels, important in the brain, heart, and ear. A CaM C-lobe calcium-dependent switch releases a shared Apo/CaM clamp conformation that enables Kv7 isoform-specific functional outcomes.

Chang et al., 2018, Neuron *97*, 836–852
February 21, 2018 © 2018 Elsevier Inc.
https://doi.org/10.1016/j.neuron.2018.01.035

CellPress

CellPress

Neuron
Article

A Calmodulin C-Lobe Ca^{2+}-Dependent Switch Governs Kv7 Channel Function

Aram Chang,[1,6] Fayal Abderemane-Ali,[1,6] Greg L. Hura,[2] Nathan D. Rossen,[1] Rachel E. Gate,[1] and Daniel L. Minor, Jr.[1,2,3,4,5,7,*]

[1]Cardiovascular Research Institute, University of California San Francisco, San Francisco, CA 94158, USA
[2]Molecular Biophysics and Integrated Bio-imaging Division, Lawrence Berkeley National Laboratory, Berkeley, CA 94720, USA
[3]Departments of Biochemistry and Biophysics, and Cellular and Molecular Pharmacology, University of California San Francisco, San Francisco, CA 94158, USA
[4]California Institute for Quantitative Biomedical Research, University of California San Francisco, San Francisco, CA 94158, USA
[5]Kavli Institute for Fundamental Neuroscience, University of California San Francisco, San Francisco, CA 94158, USA
[6]These authors contributed equally
[7]Lead Contact
*Correspondence: daniel.minor@ucsf.edu
https://doi.org/10.1016/j.neuron.2018.01.035

SUMMARY

Kv7 (KCNQ) voltage-gated potassium channels control excitability in the brain, heart, and ear. Calmodulin (CaM) is crucial for Kv7 function, but how this calcium sensor affects activity has remained unclear. Here, we present X-ray crystallographic analysis of CaM:Kv7.4 and CaM:Kv7.5 AB domain complexes that reveal an Apo/CaM clamp conformation and calcium binding preferences. These structures, combined with small-angle X-ray scattering, biochemical, and functional studies, establish a regulatory mechanism for Kv7 CaM modulation based on a common architecture in which a CaM C-lobe calcium-dependent switch releases a shared Apo/CaM clamp conformation. This C-lobe switch inhibits voltage-dependent activation of Kv7.4 and Kv7.5 but facilitates Kv7.1, demonstrating that mechanism is shared by Kv7 isoforms despite the different directions of CaM modulation. Our findings provide a unified framework for understanding how CaM controls different Kv7 isoforms and highlight the role of membrane proximal domains for controlling voltage-gated channel function.

INTRODUCTION

Kv7 (KCNQ) voltage-gated potassium channels (Kv7.1–Kv7.5) (Gutman et al., 2003) produce the neuronal M-current (Kv7.2–Kv7.5) (Delmas and Brown, 2005; Hernandez et al., 2008; Wang et al., 1998) and the I_{KS} current in heart, vestibular, and auditory cells (Kv7.1) (Barhanin et al., 1996; Jentsch, 2000; Sanguinetti et al., 1996; Wang et al., 1996). Kv7s open at subthreshold membrane potentials and place a strong brake on membrane excitation. Consequently, they sit at a key point for excitability control in both the brain and heart. Accordingly, more than 300 Kv7 mutations have been linked to diseases, such as arrhythmia, deafness, and epilepsy (Jentsch, 2000; Maljevic et al., 2010; Soldovieri et al., 2011).

Kv7s are assembled from four transmembrane subunits having the classic voltage-gated potassium channel architecture (Sun and MacKinnon, 2017) in which each subunit has six transmembrane helices. Four, S1–S4, form the voltage-sensor domain (VSD), while the last two, S5–S6 form the pore domain. This canonical transmembrane architecture is followed by a cytoplasmic C-terminal domain (CTD) that constitutes about half of the protein (Haitin and Attali, 2008) and that is central to channel assembly, gating, and modulation by calmodulin (CaM) (Gamper and Shapiro, 2003; Ghosh et al., 2006; Shamgar et al., 2006; Wen and Levitan, 2002; Yus-Najera et al., 2002). The CTD has four helical segments, denoted A–D. The most distal, the D helix, forms a four-stranded coiled coil that is important for tetramerization and subunit assembly specificity (Howard et al., 2007; Wiener et al., 2008). The two segments closest to the pore, the A and B helices, comprise the CaM interaction site (Sachyani et al., 2014; Strulovich et al., 2016; Sun and MacKinnon, 2017; Xu et al., 2013).

CaM strongly modulates Kv7 function (Gamper and Shapiro, 2003; Ghosh et al., 2006; Shamgar et al., 2006; Sihn et al., 2016; Wen and Levitan, 2002; Yus-Najera et al., 2002) by acting as a calcium sensor (Gamper and Shapiro, 2003; Sihn et al., 2016) and binds to Kv7s in both Apo/CaM and Ca^{2+}/CaM forms (Bal et al., 2008; Liu and Devaux, 2014; Wen and Levitan, 2002; Xu et al., 2013; Yus-Najera et al., 2002). Disruption of CaM interactions with Kv7.1 (Ghosh et al., 2006; Shamgar et al., 2006), Kv7.2 (Etxeberria et al., 2008), and the Kv7.2/Kv7.3 heteromer (Liu and Devaux, 2014) by disease mutations has indicated that CaM-Kv7 complex formation is important for channel assembly and trafficking and, together with other studies, support the idea that CaM is an auxiliary subunit (Etxeberria et al., 2008; Gamper et al., 2005; Gamper and Shapiro, 2003; Ghosh et al., 2006; Levitan, 2006; Shamgar et al., 2006; Wen and Levitan, 2002; Yus-Najera et al., 2002). Nevertheless, the exact mechanism by which CaM controls channel function has remained unresolved. Further, the apparently different effects of Ca^{2+}/CaM on the neuronal isoforms (Kv7.2–7.5) versus the predominantly cardiac isoform Kv7.1 have eluded a clear

mechanistic explanation (Delmas and Brown, 2005; Gamper et al., 2005; Gomis-Perez et al., 2017; Jespersen et al., 2005; Sachyani et al., 2014; Tobelaim et al., 2017b).

We previously proposed that CaM acts as a Ca^{2+}-dependent switch between a bidentate-bound Apo/CaM form, spanning the A and B helices, and a Ca^{2+}/CaM form bound to the B helix (Xu et al., 2013). Recent structural studies of CaM complexes have found a range of bidentate CaM/AB domain complexes having varied divalent-bound configurations including CaM:Kv7.1 AB domain complexes having a Ca^{2+}/N-lobe and Apo/C-lobe in 5 mM $CaCl_2$ and 1 mM EGTA conditions (Sachyani et al., 2014), a Ca^{2+}/CaM:Kv7.2/7.3 AB domain chimera (Strulovich et al., 2016), and a CaM:Kv7.1 complex in which EF hands EF1, EF2, and EF4 are occupied by divalent ions (Sun and MacKinnon, 2017). These structural observations seemingly run counter to the proposed Apo/CaM-Ca^{2+}/CaM switch (Xu et al., 2013). However, the observation of a CaM-clamp conformation in isoforms having different CaM responses, Kv7.1 and Kv7.2/7.3, fails to account how a common structure could underlie the differences in the effects of CaM modulation on Kv7.1 versus the neuronal isoforms Kv7.2–Kv7.5 (Delmas and Brown, 2005; Jespersen et al., 2005). Further, a structure of an authentic Apo/CaM-bound form has remained elusive. Hence, whether different types of CaM-Kv7 interactions govern the modulation of different Kv7 isoforms or whether there are different transduction mechanisms arising from a common CaM-channel interaction scaffold has been unresolved.

Here, using structural studies of CaM:Kv7 AB domain complexes from Kv7.4 and Kv7.5, we provide multiple lines of evidence that support a unified mechanism for Kv7 modulation by CaM. The core of this regulatory mechanism uses a switch between a cross-bridged Apo/CaM state and release of this cross-bridge caused by Ca^{2+} binding to the CaM C-lobe. Two observations are central to this mechanism. The Apo/C-lobe is in a "semi-open" conformation that can be opened by Ca^{2+} binding, whereas the CaM N-lobe remains anchored in the same position on the B helix in both the Apo- and Ca^{2+}-bound forms, adopting an "open" binding pose on the B helix in the Apo state that is essentially identical to the Ca^{2+}-bound form, except for the lack of Ca^{2+} ions. Because the Apo/N-lobe is pre-organized into a conformation identical to Ca^{2+}/N-lobe, Ca^{2+} binding is able to increase the N-lobe:B helix affinity and thereby allow the N-lobe to stay anchored on the B helix when C-lobe:A helix interactions are disrupted. Notably, we find that the C-lobe EF3, a site that has been observed to lack divalent ions even when the other three EF hands are occupied (Sun and MacKinnon, 2017), has a particularly important role in driving the C-lobe switch. Further, the C-lobe switch controls the function of both Kv7.4 and Kv7.1 despite affecting channel opening in opposite ways. Hence, the C-lobe switch uses a common mechanism arising from a shared scaffold regardless of how changes in this modulatory unit are coupled to channel opening.

RESULTS

Crystal Structure of the Apo/CaM:Kv7.4 AB Domain Complex

We co-expressed, purified, and crystallized an Apo/CaM:Kv7.4 AB domain complex. Similar to prior Kv7 AB domain studies (Sachyani et al., 2014; Strulovich et al., 2016), deletion of much of the poorly conserved AB linker, Kv7.4 residues 368–523 (Figure S1A), was necessary and yielded a well-behaved 1:1 CaM:Kv7.4 AB domain complex over a wide range of concentrations as judged by size exclusion chromatography (SEC)-multiangle light scattering (MALS) (Figure S1B). In agreement with prior deletion studies of Kv7.1 (Haitin et al., 2009), the AB linker truncation did not affect channel function and improved channel expression (Figures S1C and S1D). Following purification in 1 mM EGTA, crystals were grown that diffracted X-rays to 2.30 Å resolution (Table S1), and the structure was determined by single anomalous diffraction-molecular replacement (SAD-MR) using an isomorphous heavy atom derivative with Di-μ-iodobis(ethylenediamine)diplatinum(II) nitrate ($[Pt_2I_2(H_2NCH_2CH_2NH_2)_2](NO_3)_2$). Structure determination revealed four 1:1 Apo/CaM:Kv7.4 AB domain complexes per asymmetric unit (Figure S1E). In each, one CaM embraces an antiparallel helical pair of Kv7.4 A and B helices from a single AB domain (Figure 1A). All asymmetric unit complexes adopt similar conformations having a root mean square deviation, Cα ($RMSD_{C\alpha}$) of <0.300 Å (Figure S2A). This conformation differs dramatically from the Ca^{2+}/CaM:Kv7.4 B helix complex (Figure 1B) (Xu et al., 2013), and, unlike prior Kv7 AB domain complexes (Sachyani et al., 2014; Strulovich et al., 2016; Sun and MacKinnon, 2017), all four CaM EF hands lack bound divalent ions (Figure S3) consistent with the constant presence of 1 mM EGTA.

The Kv7.4 AB domain comprises three helices. The A helix, residues His330-Met357, the B helix, residues Pro528-Arg554, and a short helix formed by the AB-linker Ala364-Met527 (Figures 1A and S1A). There is a small difference in the extent of helical structure of the N-terminal end of the A helix in the different copies of the asymmetric unit (Figures S1A and S1F). As with the CaM:Kv7.1 AB domain complex structures (Sachyani et al., 2014; Sun and MacKinnon, 2017) and the CaM:Kv7.3 A helix/Kv7.2 B helix complex (Strulovich et al., 2016), CaM C-lobe binds the Kv7.4 A helix and the CaM N-lobe binds the Kv7.4 B helix through an extensive set of contacts (Figures S4A and S4B).

The Apo/CaM N-lobe adopts an open conformation (Meador et al., 1992) that is essentially identical to that of Ca^{2+}/CaM N-lobe (Figure 2A). This open Apo/N-lobe conformation is unlike previously observed target-bound Apo/N-lobe conformations (Houdusse et al., 2006; Lu et al., 2015) and binds the Kv7.4 B helix in a manner matching the Ca^{2+}/CaM N-lobe:Kv7.4 B helix complex (Xu et al., 2013) (RMSD = 0.449 Å, $RMSD_{C\alpha}$ = 0.375 Å) using the same principal anchor residues, Val533, Ser536, Ile537, Ile539, and Leu540 (Figure 1C) and burying a similar amount of surface area (1,900 and 1,870 $Å^2$, respectively for the Apo/CaM N-lobe and Ca^{2+}/CaM N-lobe). The conformational differences between the Apo/CaM N-lobe and Ca^{2+}/CaM N-lobe reside in the EF1 X, Y, and Z ligands, Asp20, Asp22, and Asp24 as well as more distributed differences in EF2 (Figures 2B, S5A, and S5B). These differences result in an EF hand pair in which the calcium-coordinating ligands are not arranged to coordinate calcium agreeing with the observed Apo/N-lobe state.

By contrast to the strong similarity between the Apo/N-lobe and Ca^{2+}/N-lobe in the Kv7.4 AB domain and B helix complexes,

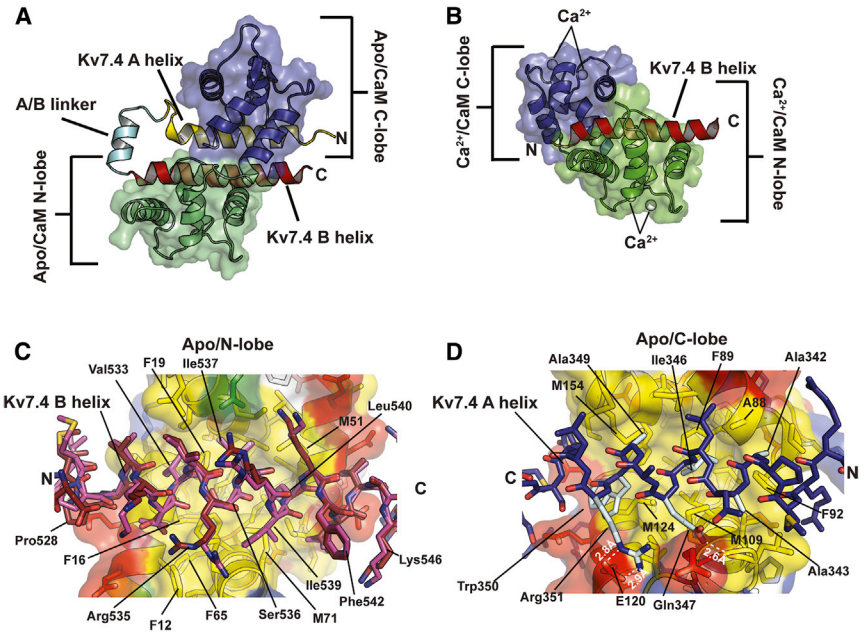

Figure 1. Structure of the Apo/CaM:Kv7.4 AB Domain Complex

(A) Apo/CaM:Kv7.4 AB domain complex cartoon diagram. Apo/CaM N-lobe and Apo/CaM C-lobe are shown as semitransparent surface in green and blue, respectively. Kv7.4 A helix, AB linker, and B helix region are colored yellow, cyan, and red, respectively.

(B) Ca^{2+}/CaM:Kv7.4 B helix complex (PDB: 4GOW) (Xu et al., 2013) cartoon diagram. Ca^{2+}/CaM N-lobe and Ca^{2+}/C-lobe are green and blue, respectively. Kv7.4 B helix is red.

(C) Apo/N-lobe:Kv7.4 B helix interaction. Apo/CaM:Kv7.4 AB domain Kv7.4 B helix (magenta) and Ca^{2+}/CaM:Kv7.4 B helix (firebrick) are superposed. Apo/CaM:Kv7.4 AB domain Kv7.4 B helix anchors are colored pink.

(D) Apo/C-lobe:Kv7.4 A helix interaction. Kv7.4 A helix is colored dark blue having light blue anchor residues. Hydrogen bonds are indicated by white dashed lines.

In (C) and (D), Apo/CaM lobes are shown as semitransparent surface and stick. Hydrophobic, acidic, basic, and polar residues are colored yellow, red, blue, and green, respectively. Select residues are labeled using three-letter code for Kv7.4 and single-letter code for Apo/CaM.

See also Figures S1–S4 and S7 and Tables S1 and S2.

there are stark differences between the Apo/C-lobe and Ca^{2+}/C-lobe conformations (RMSD = 3.860 Å) (Figures 2C, 2D, S5C, and S5D). Apo/C-lobe assumes a semi-open form that is very similar to the conformation of the Apo/CaM C-lobe in the Myosin V complex (RMSD = 0.768 Å) (Houdusse et al., 2006) (Figures 2E and 2F) and that has notable differences in the E helices of both EF hands (Figure 2F). The Kv7.4 A helix engages the Apo/C-lobe through interactions with a set of five hydrophobic residues, Ala342, Ala343, Ile346, Ala349, and Trp350, augmented by a bidentate electrostatic interaction between Arg351 and CaM Glu120 and a hydrogen bond between Gln347 and the CaM Leu112 backbone carbonyl (Figure 1D). This interaction surface is much larger than the Ca^{2+}/C-lobe Kv7.4 B helix interaction (2,180 versus 1,120 $Å^2$) and comparable to the Apo/C-lobe Myosin V interaction (1,918 $Å^2$). Ile346 is part of the A helix "IQ" motif (Yus-Najera et al., 2002) and is buried deeply in an Apo/C-lobe pocket comprising Ala88, Phe89, Phe92, Met109, and Met124. The correspondence of the Apo/C-lobe:Kv7.4 A helix IQ domain interactions with those made by the IQ motif in the Apo/CaM:Myosin V complex (Houdusse et al., 2006) is striking (Figure S5E). Aside from the identical IQ residue poses, many other side chains on each of the IQ helices adopt similar conformations against the Apo/C-lobe surface (Figure S5E), underscoring a common structural basis for IQ motifs as Apo/CaM anchoring sites (Bähler and Rhoads, 2002; Rhoads and Friedberg, 1997; Tidow and Nissen, 2013).

Divalent Ions Can Occupy N-Lobe EF Hands in the CaM:Kv7.4 AB Domain Complex

Previous CaM:Kv7 AB domain complexes of Kv7.1 (Sachyani et al., 2014; Sun and MacKinnon, 2017) and the Kv7.3/7.2 AB domain chimera (Strulovich et al., 2016) showed N-lobe bound calcium ions that persisted even when extreme measures were taken to remove them (Sachyani et al., 2014). As we were able to crystallize an authentic Apo/CaM form, we tried to observe the transition from the Apo/CaM state to a calcium-bound state. Soaking the Apo/CaM:Kv7.4 AB domain crystals for as short as 1 hr with a 10 μM $CaCl_2$ solution caused the crystals to dissolve, suggesting that calcium induced a conformational change. This was not true for soaks with Mg^{2+}, a divalent ion that binds CaM but does not drive CaM conformational changes (Grabarek, 2011). However, the Apo/CaM:Kv7.4 AB domain crystals were able to survive shorter calcium soaks. By using a 1 min soaking procedure for 10 μM and 1 mM $CaCl_2$, and 1 mM $MgCl_2$, we were able to obtain datasets at 2.20, 2.30, and 2.20 Å resolution, respectively, that were solved by molecular replacement (Table S1; Figures S2A, S2B, S6A, S6C, and S6E).

Structure solution revealed clear density for a calcium ion in all four copies of EF1 for the 10 μM soak making a hemi-occupied lobe (Hemi/N-lobe) (Figures S6A and S6B) and density in both EF1 and EF2 for the 1 mM soak making Ca^{2+}/N-lobe (Figures S6C and S6D). Magnesium occupied EF1 in all four copies of the $MgCl_2$ soak (Figures S6E and S6F). There were clear rearrangements in EF1 calcium-coordinating residues D22 (Y), D24 (Z) T28 (–X), E31 (–Z) in both the 10 μM and 1 mM Ca^{2+} structures (Figures 3A and 3B) and in EF2 residues D58 (Y), N60 (Z), T62 (–Y), D64 (–X), E67 (–Z) (Figure 3B). In each case, the movements are consistent with formation of a calcium coordination sphere. These data support the assignment of the Apo/CaM N-lobe as lacking divalents and are consistent with the high overall similarity of the Apo/CaM and Ca^{2+}/CaM N-lobe conformations (Figures 2A and 2B). They also show that only small conformational changes are required to accommodate calcium

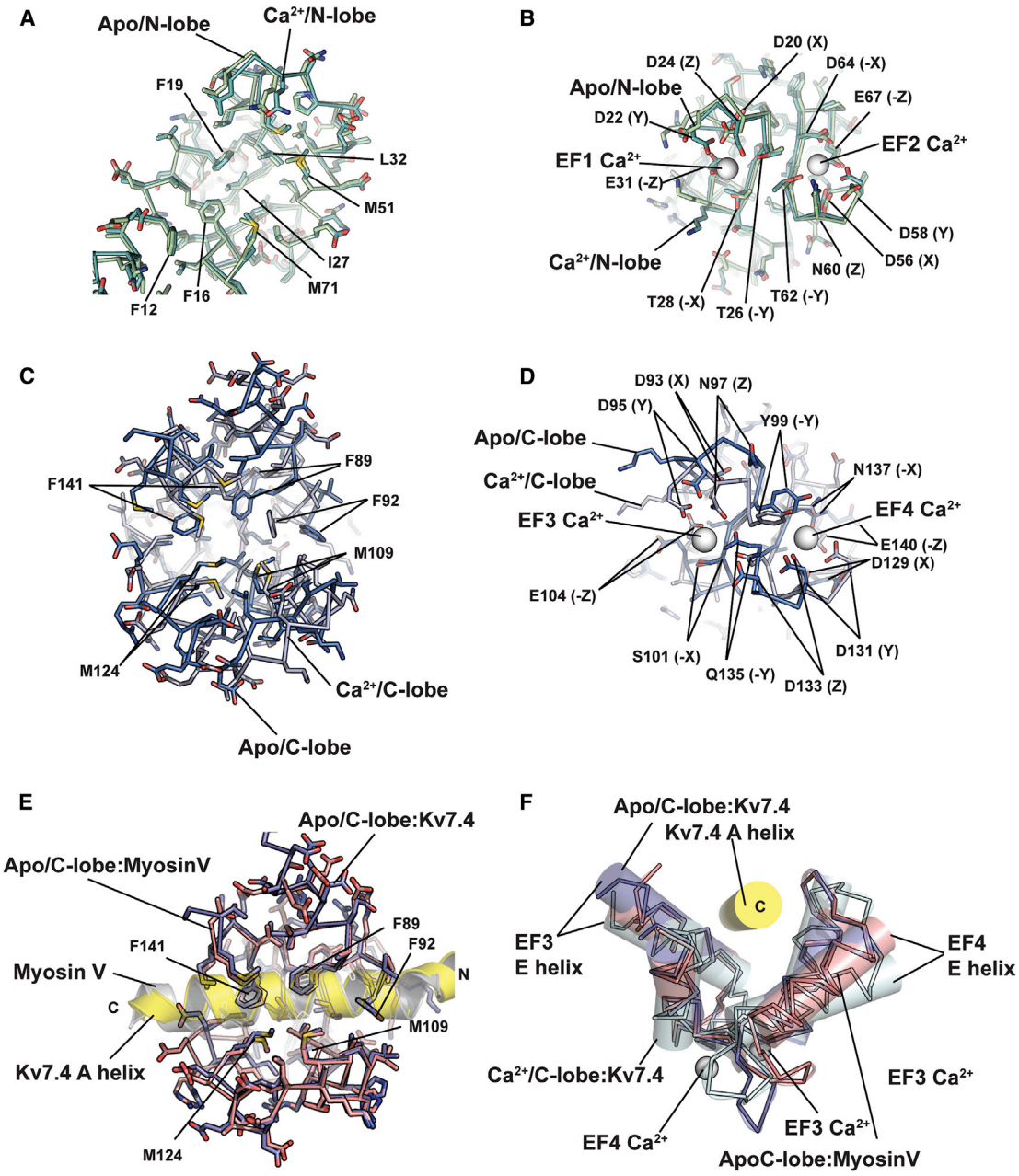

Figure 2. Structural Comparisons of Apo/CaM and Ca^{2+}/CaM Lobes and IQ Motif Binding

(A) View of the B helix binding pocket of superposed Apo/N-lobe (pale green) and Ca^{2+}/N-lobe (cyan) (4GOW) (Xu et al., 2013).

(B) View of the N-lobe EF hand domains from (A). Calcium binding residues are labeled. Canonical EF hand labels are in parentheses.

(C) Ligand binding pocket view of superposed Apo/C-lobe (marine) and Ca^{2+}/C-lobe (light blue) (4GOW) (Xu et al., 2013).

(D) View of the C-lobe EF hands from (C). Calcium binding residues are labeled. Canonical EF hand labels are in parentheses.

(E) Comparison of Apo/CaM:Kv7.4 AB domain and Apo/CaM:Myosin V complex (2IX7) (Houdusse et al., 2006) Apo/C-lobe binding modes. Apo/C-lobe of the Kv7.4 AB domain (marine) and Myosin V (salmon) complexes are shown as sticks. Kv7.4 A helix (yellow) and Myosin V helix (white) are shown as cartoons. Select Apo/CaM residues are labeled.

(F) Side view of (E) (purple) showing the Apo/CaM elements as wires and cylinders and Kv7.4 A and Myosin V helices as cylinders. EF hand elements are labeled. See also Figures S2 and S5 and Table S2.

binding and that calcium ions can be bound in the CaM N-lobe EF hands while maintaining the clamp structure. Notably, loading of the N-lobe rather than the C-lobe runs opposite to the intrinsic affinities of the individual lobes for calcium (Linse et al., 1991) and suggests that the calcium affinities of the individual lobes in the Kv7.4 AB domain complex are tuned by binding partner

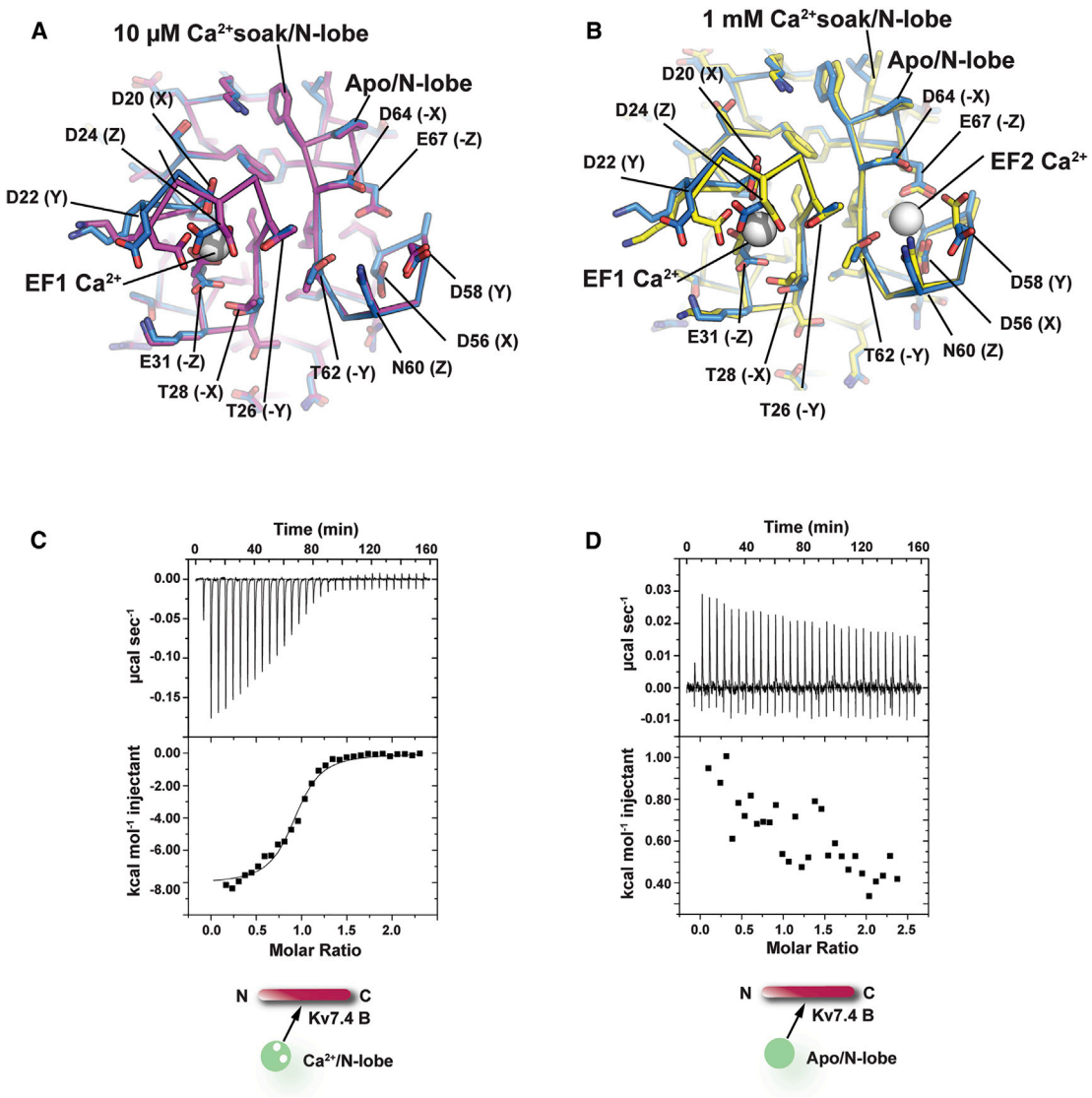

Figure 3. CaM N-Lobe EF Hand Structure and Calcium-Dependent Binding Properties

(A) Apo/N-lobe (marine) and 10 μM $CaCl_2$-soaked N-lobe (violet).

(B) Apo/N-lobe (marine) and 1 mM $CaCl_2$-soaked N-lobe (yellow). Ca^{2+} ions are white spheres.

(C) Titration of 7.5 μM Ca^{2+}/N-lobe into 75 μM Kv7.4 B-peptide. Measured thermodynamic parameters are N = 0.86 ± 0.02; $K_a = 4.67 \times 10^6 \pm 1.22 \times 10^6$ M^{-1}; $\Delta H = -8.04$ kcal mol^{-1} ± 0.28; $\Delta S = 2.53$ cal mol^{-1} deg^{-1}; n = 2.

(D) Titration of 7.5 μM Apo/N-lobe into 75 μM Kv7.4 B-peptide. No binding detected indicating a K_a of $<1 \times 10^5$. Error bars are SEM.

See also Figures S2 and S6 and Tables S1 and S2.

interaction as in other CaM complexes (Evans and Shea, 2009; Findeisen et al., 2013; Xia and Storm, 2005).

Differential Binding of CaM N-Lobe to the B Helix

Given the small structural differences between the structures of the Apo/N-lobe:Kv7.4 B helix and Ca^{2+}/N-lobe:Kv7.4 B helix complexes, we asked whether calcium ions affected the strength of this interaction. Isothermal titration calorimetry (ITC) experiments showed that Ca^{2+}/N-lobe binds the Kv7.4 B helix tightly (K_d = 210 nM) (Figure 3C). By contrast, we could not measure Apo/N-lobe binding (Figure 3D). These results indicate an affinity difference between the Ca^{2+}/N-lobe and Apo/N-lobe of >50-fold. Attempts to use ITC to examine other interactions were complicated by complex binding isotherms (e.g., full-length CaM:B helix) and lack of isolated A-peptide stability. We note that these direct thermodynamic binding measurements differ from results using fluorescence approaches (Alaimo et al., 2014). Nevertheless, these data together with the structural observations that the N-lobe is pre-organized into a calcium-bound-like conformation (Figures 2A and 2B) and the observation that Apo/CaM binding to the Kv7.4 CTD depends on the Kv7.4 A helix (Xu et al., 2013) indicate that the clamped Apo/CaM

structure is important for stabilizing the N-lobe:B helix interactions. Hence, both the Apo/C-lobe and Apo/N-lobe interactions contribute to Apo/CaM binding. Moreover, the data show that calcium binding causes a large gain in the ability of the N-lobe to bind the B helix independently of other interactions.

Apo/CaM Clamp Is Maintained in High Magnesium

We also obtained crystals of a Kv7.5 AB domain construct similar to the Kv7.4 AB domain (Figure S1A) in the presence of 200 mM Mg^{2+} and in a different crystal form ($P2_12_12_1$ versus $I222$) from the Kv7.4 AB domain that diffracted to 2.60 Å resolution (Table S1). Structure solution, by molecular replacement using the Apo/CaM:Kv7.4 AB domain, revealed four identical copies per asymmetric unit (Figures S2C and S7A) having an overall structure very similar to the Apo/CaM:Kv7.4 complexes (RMSD = 0.688 Å, $RMSD_{C\alpha}$ = 0.596 Å) (Table S2) having one CaM that binds the Kv7.5 A and B helices using the C-lobe and N-lobe, respectively. The Kv7.5 AB linker makes an irregular loop structure rather than a helix as in the Apo/CaM:Kv7.4 structure (Figures 1A and S7B). The two CaM lobes bind the Kv7.5 A and B helices using residues Val521, Ala524, Ile525, Ile527, Met528 to engage the Mg^{2+}/N-lobe and five hydrophobic anchors, Ala370, Ala371, Ile374, Val377, and Trp378, together with hydrophilic interactions made by Gln375 and Arg379 to bind the Mg^{2+}/C-lobe (Figures S4C, S4D, S7C, and S7D). Both sets of interactions match those in the Apo/CaM:Kv7.4 complex (Figures S4C, S4D, S7E, and S7F), and, accordingly, the Kv7.5 AB domain complex CaM lobes bury surface areas comparable to the Kv7.4 complex (1,920 and 1,900 $Å^2$ for the Kv7.5:N-lobe and Kv7.4:N-lobe interactions, respectively, and 2,430 and 2,180 $Å^2$ for Kv7.5:C-lobe and Kv7.4:C-lobe interactions, respectively). EF1, EF2, and EF4 displayed density consistent with the presence of a Mg^{2+} with one copy also having density for Mg^{2+} in EF3 (Figures S7A and S7G). Together, these data show an essentially Apo/CaM like structure in which the C-lobe adopts a semi-open conformation, whereas the N-lobe is in the open conformation despite the lack of an activating ion, further supporting the idea that the N-lobe/Kv7 B helix interactions pre-organize the N-lobe into a calcium-binding competent conformation.

Comparison to CaM:Kv7.1 AB Domain and CaM:Kv7.2/7.3 AB Domain Chimera Structures

The CaM:Kv7.4 and CaM:Kv7.5 AB domain complexes share the global architecture seen in the CaM:Kv7.1 AB domain complexes (Sachyani et al., 2014; Sun and MacKinnon, 2017) and CaM: Kv7.3 A/Kv7.2 B domain complex (Strulovich et al., 2016) ($RMSD_{C\alpha}$ = 1.567, 1.317, 1.490 Å, Apo/CaM:Kv7.4; 1.536, 1.364, 1.409 Å Mg^{2+}CaM:Kv7.5 versus Kv7.1 (Sachyani et al., 2014), Kv7.1 full-length (Sun and MacKinnon, 2017), and Kv7.2/7.3 complexes (Strulovich et al., 2016), respectively) (Figures 4A–4D and S8; Table S2). The Kv7.4 and Kv7.5 AB domain complexes all have the *cis*-configuration in which CaM engulfs the A and B helices from the same chain that is found in the CaM:Kv7.1 AB domain complex in the context of the full channel (Sun and MacKinnon, 2017) and CaM:Kv7.3 A/Kv7.2 B domain complex (Strulovich et al., 2016).

Differences between the Kv7.4 AB domain complexes and the Kv7.1 AB domain and Kv7.3/7.2 AB domain complexes occur in the EF hand ion binding sites, which are empty in the Apo/CaM:Kv7.4 AB domain complex. In the CaM:Kv7.1 AB domain complex crystal structure, the N-lobe EF hands contain calcium ions, whereas the C-lobe EF hands lack bound divalents (Sachyani et al., 2014). This Ca^{2+}/N-lobe matches what we observe for the 1 mM $CaCl_2$ soaks of the Apo/CaM:Kv7.4 AB domain complex (Figure 3B). Cryoelectron microscopy (cryo-EM) studies of a CaM:Kv7.1 complex identified divalent ions in EF hands 1, 2, and 4 and an empty EF3 (Sun and MacKinnon, 2017). Accordingly, its major difference with the Kv7.4 complex is in the EF4 conformation resulting from the bound ion. By contrast, both Apo/EF3s show close agreement (Figure S8). The CaM:Kv7.3 A helix/Kv7.2 B helix chimera complex structure (Strulovich et al., 2016) has calcium ions in all four CaM EF hands. Nevertheless, the overall lobe conformations match the open and semi-open N-lobe and C-lobe conformations seen in the Apo/CaM:Kv7.4 complex. The N-lobe:B helix and C-lobe:A helix interactions in the Apo/CaM:Kv7.4 and Mg^{2+}/CaM:Kv7.5 complexes are almost identical to the other isoforms (Figures 4C and 4D) (Apo/N-lobe:Kv7.4 B helix, $RMSD_{C\alpha}$ = 0.781 and 0.601 Å versus Kv7.1 and Kv7.2/7.3; Mg^{2+}/N-lobe:Kv7.5 $RMSD_{C\alpha}$ = 0.579 and 0.664 Å for Kv7.1 and Kv7.2/7.3; Apo/C-lobe:Kv7.4 A helix, $RMSD_{C\alpha}$ = 0.605 and 0.403 Å versus Kv7.1 and Kv7.2/7.3; Mg^{2+}/C-lobe:Kv7.5 A helix, $RMSD_{C\alpha}$ = 0.816 and 0.799 Å versus Kv7.1 and Kv7.2/7.3).

There are conformational differences in the N-terminal portion of the A helix that extends beyond the CaM complex, the AB linkers, and the length of the N-terminal portion of the Kv7.1 B helix (Figure 4B). Differences in the A helix N-terminal end are similar to those among the CaM:Kv7.4 AB domain complexes (cf. Figures S1F, S6A, S6C, and S6E) and suggest that this region is flexible. The N-terminal end of the Kv7.2, Kv7.4, and Kv7.5 B helices begin at a conserved proline (Pro534, Pro528, and Pro516, respectively). This position is a glutamate Kv7.1, and this difference likely supports the longer Kv7.1 helix given the low helix propensity of proline (O'Neil and DeGrado, 1990).

Taken together, the similarities in CaM:Kv7 AB domain interactions underscore the commonality of CaM clamp interaction among Kv7 isoforms. The compatibility of this mode with a variety of calcium-bound states suggests that, in conditions where constraints are imposed either by the crystal lattice or by interactions within the full-length complex, it is possible to maintain the clamp. Thus, the structures raise the key question of how this common structure is related to Kv7 function.

Calcium Causes a Conformational Change in the CaM/Kv7.4 A-B Domain Complex

Although the CaM clamp structure can be maintained in some cases when divalent ions are bound to the EF hands, addition of calcium to the Apo/CaM:Kv7.4 AB domain complexes led to crystal dissolution, suggesting a calcium-dependent conformational change. To explore this possibility, we used small-angle X-ray scattering (SAXS). We examined a Kv7.4 CTD construct spanning the A–D elements, but lacking part of AB linker, denoted Kv7.4 AD(Δ368–492) (Xu et al., 2013). Similar to the longer crystal construct deletion, this AB linker deletion was necessary to obtain a well-behaved sample but did not affect function (Figures S1C and S1D). SAXS experiments under

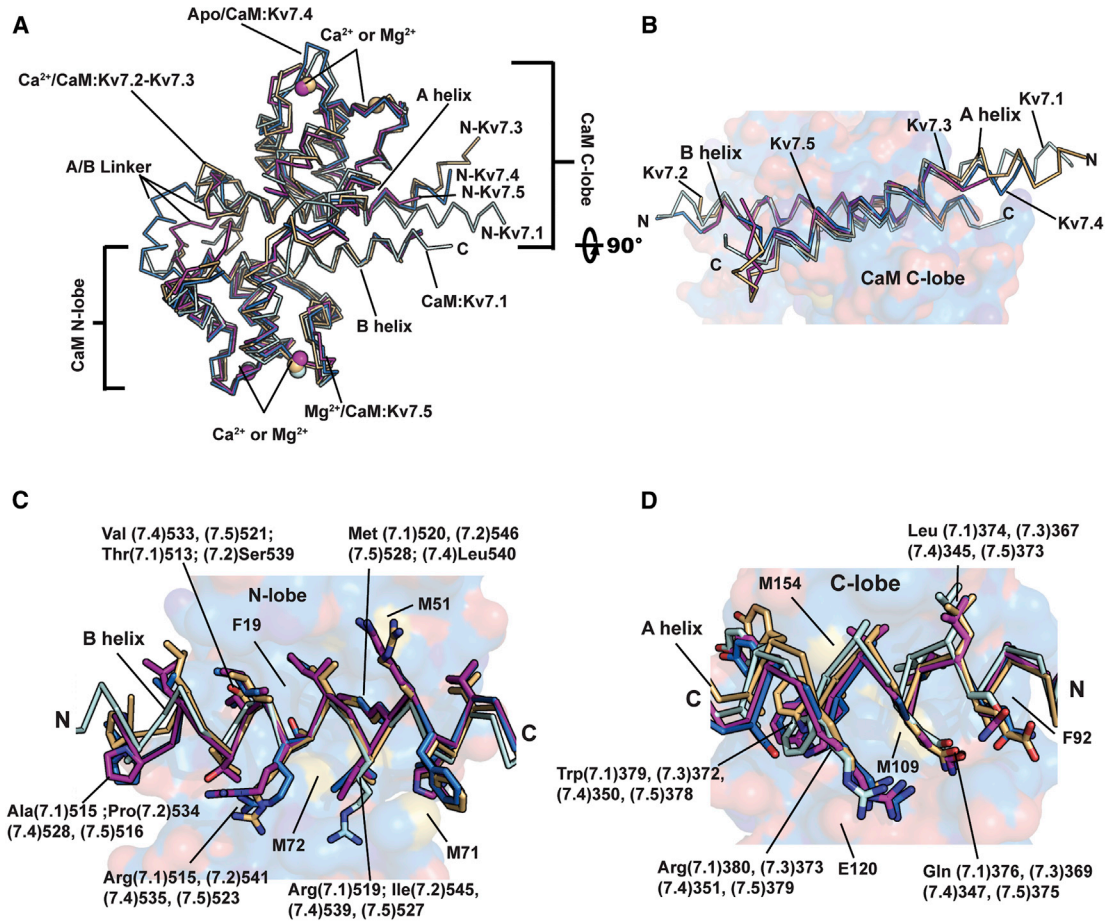

Figure 4. CaM:Kv7 AB Domain Structure Comparisons

(A) Wire diagram superposition of AB domain complexes for Apo/CaM:Kv7.4 (marine), Mg^{2+}/CaM:Kv7.5 (magenta), hemi-CaM:Kv7.1 (cyan) (Sachyani et al., 2014), and Ca^{2+}/CaM:Kv7.2/7.3 (light orange) (Strulovich et al., 2016). Divalent ions are shown as spheres.

(B) A and B helices from (A). Kv7.4 complex Apo/CaM is shown as a surface.

(C and D) View of (C) N-lobe:Kv7 B helix and (D) C-lobe:Kv7 A helix from (A). Select residues are shown as sticks and labeled with three-letter code. Parentheses indicate Kv7 isoform. Apo/N-lobe and Apo/C-lobe from the Kv7.4 complex are shown as a semitransparent surface. Select CaM residues are labeled using single-letter code. Nitrogen, oxygen, and sulfur atoms are colored blue, red, and yellow, respectively.

See also Figures S1, S2, S4, and S8 and Tables S1 and S2.

low- and high- calcium conditions showed striking differences in size and flexibility of the Apo/CaM:Kv7.4 AD and Ca^{2+}/CaM:Kv7.4 AD states (Figures 5A and 5B; Table S3) that were apparent from the stark differences in the Porod volume and values, which are bounded by 4 for rigid and 2 for completely flexible structures (Hammel, 2012; Rambo and Tainer, 2011)). These data, together with the presence of the clear plateau for Apo/CaM:Kv7.4 AD that is not found for the calcium-bound form Ca^{2+}/CaM:Kv7.4 AD (Figure 5B), indicate that Apo/CaM:Kv7.4 AD(Δ368–492) has compact structure and that Ca^{2+}/CaM:Kv7.4 AD(Δ368–492) is larger and more flexible. Additionally, we observed differences in the size of the complex as judged by D_{max} values from the pair distance distribution, P(r) analysis (Figure 5D; Table S3) and the radius of gyration (D_{max} 135 versus 149 Å, R_g 44.7 versus 49.5 Å for Apo/CaM:Kv7.4 AD and Ca^{2+}/CaM:Kv7.4 AD, respectively). Notably, similar analysis using a complex lacking the A-domain in the presence of calcium, Ca^{2+}/CaM:Kv7.4 BD reveals a compact complex having size and Porod values similar to the Apo/CaM:Kv7.4 AD complex (D_{max} 131 versus 135 Å, R_g 45.2 versus 44.7 Å for Ca^{2+}/CaM:Kv7.4 BD and Apo/CaM:Kv7.4 AD, respectively) and different from the Ca^{2+}/CaM:Kv7.4 AD complex (Figures 5C and 5D; Table S3). These data indicate that the differences between Apo/CaM:Kv7.4 AD and Ca^{2+}/CaM:Kv7.4 AD arise from changes in the A-domain. Taking into consideration the Apo/CaM:Kv7.4 AB domain and Ca^{2+}/CaM:Kv7.4 B helix crystal structures, these results suggest that there is a calcium-driven conformational switch between the clamped Apo/CaM form structure that engulfs the A and B helices, and the Ca^{2+}/CaM form, which binds only to the B helix and in which the A helix is released and becomes disordered (Figure 5E) as previously proposed (Xu et al., 2013). This interpretation is further supported by the affinity change in CaM N-lobe for the B helix (Figures 3C and 3D) and provide an explanation for how the

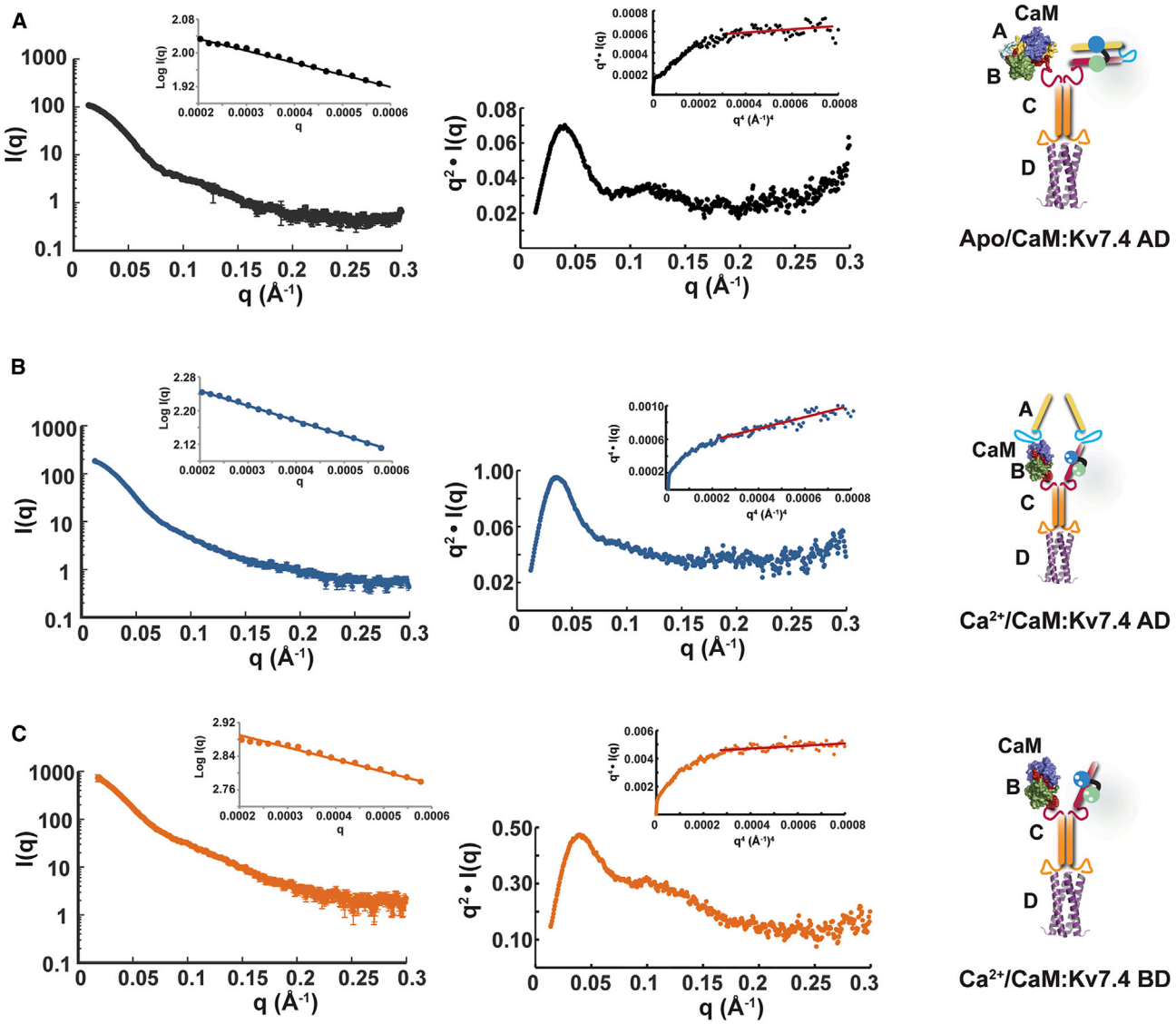

(legend on next page)

CaM N-lobe can remain in place while the C-lobe changes positions between the Apo- and Ca^{2+}-bound forms (Movie S1).

Ca^{2+}-Dependent C-Lobe Interactions Modulate Kv7.4 Activation

We sought to test whether the clear calcium-dependent structural properties of the CaM:Kv7.4 complexes had functional correlates. Hence, we measured Kv7.4 activity in presence of CaM or CaM mutants that disabled the calcium binding ability of the N-lobe (CaM_{12}), the C-lobe (CaM_{34}), or both (CaM_{1234}) (Keen et al., 1999). Electrophysiology using the perforated patch configuration to avoid major cytosolic composition changes revealed that co-expression of CaM_{1234}, an Apo/CaM mimic, accelerated the fast component of Kv7.4 channel activation (τ at 0 mV = 133.9 ± 9.8 ms Kv7.4:CaM; 39.0 ± 4.3 ms Kv7.4:CaM_{1234}) (Figures 6A and 6B), sparing deactivation (Figure S9A), and produced a large (>35 mV) leftward shift in the voltage dependence of activation ($V_{1/2}$ = −12.4 ± 2.2 mV, Kv7.4:CaM; −49.2 ± 3.4 mV, Kv7.4:CaM_{1234}) (Figure 6C; Table S4) similar to previous observations (Sihn et al., 2016). Co-expression with CaM mutants having the calcium binding ability of a single lobe impaired revealed that CaM_{34} phenocopied the effects of CaM_{1234} on both activation rate (τ at 0 mV = 43.6 ± 3.1 ms, Kv7.4: CaM_{34}) (Figures 6A and 6B) and activation voltage dependency ($V_{1/2}$ = −43.8 ± 4.9 mV, Kv7.4:CaM_{34}) (Figure 6C; Table S4). By contrast, CaM_{12} caused only modest perturbations to channel biophysical properties, producing only a slightly faster activation rate and a small activation curve leftward shift ($V_{1/2}$ = −22.4 ± 6.2 mV, Kv7.4:CaM_{12}; Table S4). Because structural studies of Kv7.1:CaM suggested a critical role for EF3 (Sun and MacKinnon, 2017), we also used individual EF hand mutants to probe the C-lobe further. These data show that the single mutant CaM_3 causes effects equivalent to CaM_{34} on both the activation rate (τ at 0 mV = 65.8 ± 6.4 ms, Kv7.4: CaM_3; 100.0 ± 4.0 ms, Kv7.4: CaM_4) (Figures 6A and 6B), and the voltage dependence of activation ($V_{1/2}$ = −42.2 ± 2.9 mV, Kv7.4:CaM_3; −34.2 ± 3.5 mV, Kv7.4:CaM_4) (Figure 6C; Table S4), whereas CaM_4 caused milder effect. These results are consistent with the possibility that Apo/EF3 contacts the S2–S3 linker from the voltage sensor domain (Sun and MacKinnon, 2017).

We also used the cell-permeant calcium chelator (1,2-Bis(2-aminophenoxy)ethane-N,N,N',N'-tetraacetic acid tetrakis (acetoxymethyl ester)) (BAPTA-AM) to reduce intracellular calcium concentrations. Application of BAPTA-AM to cells expressing Kv7.4:CaM, Kv7.4:CaM_{1234}, or Kv7.4:CaM_{34} caused changes in the fast component of activation and voltage-dependent activation properties of Kv7.4:CaM, but not Kv7.4:CaM_{1234} or Kv7.4:CaM_{34} (Figures 6D–6F; Table S4) that mirrored the effects of the co-expression of Kv7.4 with CaM_{1234} and CaM_{34} ($\tau_{(BAPTA)}$ at 0 mV = 69.1 ± 5.6 ms, Kv7.4:CaM; 42.9 ± 5.6 ms, Kv7.4:CaM_{1234}; 27.9 ± 1.2 ms, Kv7.4:CaM_{34}; $V_{1/2(BAPTA)}$ = −36.8 ± 3.7 mV Kv7.4:CaM; −39.9 ± 2.6 mV Kv7.4:CaM_{1234}; −45.2 ± 1.9 mV Kv7.4:CaM_{34}). To examine whether the cells transfected with Kv7.4 and the various CaM versions have different basal calcium levels, we used two types of calcium indicator, Fluo-3-AM and Indo-1-AM (Figure S10). These experiments showed that there was no difference among the measured calcium signals from cells transfected with Kv7.4 and the various CaM versions or from cells transfected with control voltage-gated sodium channels ($Na_V1.4$ and Na_VSp1) (Figures S9B and S10). Importantly, both BAPTA-AM and ionomycin treatment caused changes in the expected directions, depending on the indicator used. Hence, the observed functional changes are not due to variability in cytosolic calcium levels but are a direct consequence of the calcium-dependent actions of the various CaM mutants on the channel.

We also compared the effects of CaM and CaM_{1234} on Kv7.5 function (Figures S9C and S9D). In line with the Kv7.4 results and with the clamped CaM:Kv7.5 AB domain structure, we found that co-expression of the Apo/CaM mimic, CaM_{1234}, caused a leftward shift in the voltage-dependent activation of the channel ($V_{1/2}$ = −13.6 ± 4.3 mV, Kv7.5:CaM; −33.2 ± 2.1 mV, Kv7.5:CaM_{1234}). These functional consequences match the effects of CaM_{1234} on Kv7.2 (Gomis-Perez et al., 2017), Kv7.3 (Gomis-Perez et al., 2017), and Kv7.4 (Figures 6C and 6F) and demonstrate a unified mechanism in which Apo/CaM facilitates activation of the neuronal Kv7.2–Kv7.5 isoforms, whereas Ca^{2+}/CaM exerts an inhibitory effect. Taken together with the results from our structural and biophysical studies of Kv7.4, our data further indicate that CaM C-lobe acts as a Ca^{2+}-dependent switch that controls channel activity.

Because of reported differences in CaM modulation between Kv7.1 and other family members (Kv7.2–Kv7.5) (Gamper et al., 2005; Gomis-Perez et al., 2017; Sachyani et al., 2014; Tobelaim et al., 2017b) and the commonality of the CaM-clamp structures (Figure 4), we studied the effects of CaM and CaM mutants on Kv7.1. By contrast with the facilitating effects on Kv7.2–Kv7.5, Ca^{2+}-insensitive CaM mutants shifted the Kv7.1 response in the depolarizing direction, opposing channel activation. Nevertheless, similar to Kv7.4, the effect of CaM_{1234} was phenocopied completely by the C-lobe mutant CaM_{34} but not CaM_{12}, ($V_{1/2}$ = −36.4 ± 1.8 mV, Kv7.1:CaM; −25.3 ± 4.0 mV, Kv7.1:CaM_{12}; −15.4 ± 2.9 mV, Kv7.1:CaM_{34}; −13.5 ± 2.6 mV, Kv7.1:CaM_{1234}) (Figures S9E and S9F). The effects of CaM_{1234} point to an inhibitory, rather than activating role for the Apo/CaM clamp in the context of Kv7.1. Moreover, only CaM_{1234} caused a decrease in current density (Figure S9G). The functional effects on $V_{1/2}$ and current density of Kv7.1 associated with co-expression of CaM mutants differ from the results of diffusion of purified

Figure 5. SAXS Reveals Calcium-Dependent Conformational Changes in the Kv7.4 CTD

(A–C) Exemplar SAXS scattering curve with Guiner plot inset (left) and Kratky plot with Porod analysis inset (center) for (A) Apo/CaM:Kv7.4 AD, (B) Ca^{2+}/CaM:Kv7.4 AD, and (C) Ca^{2+}/CaM:Kv7.4 BD complexes. Red lines show region of Porod value determination. Icons represent the complexes.

(D) P(r) analysis for the indicated complexes.

(E) Superposition of the Apo/CaM:Kv7.4 AB domain and Ca^{2+}/CaM:Kv7.4 B helix (Xu et al., 2013) complexes showing model for the calcium-dependent switch. Orange arrow shows the change in CaM C-lobe binding between the two states. The yellow line represents the released disordered A-domain.

See also Movie S1 and Table S3.

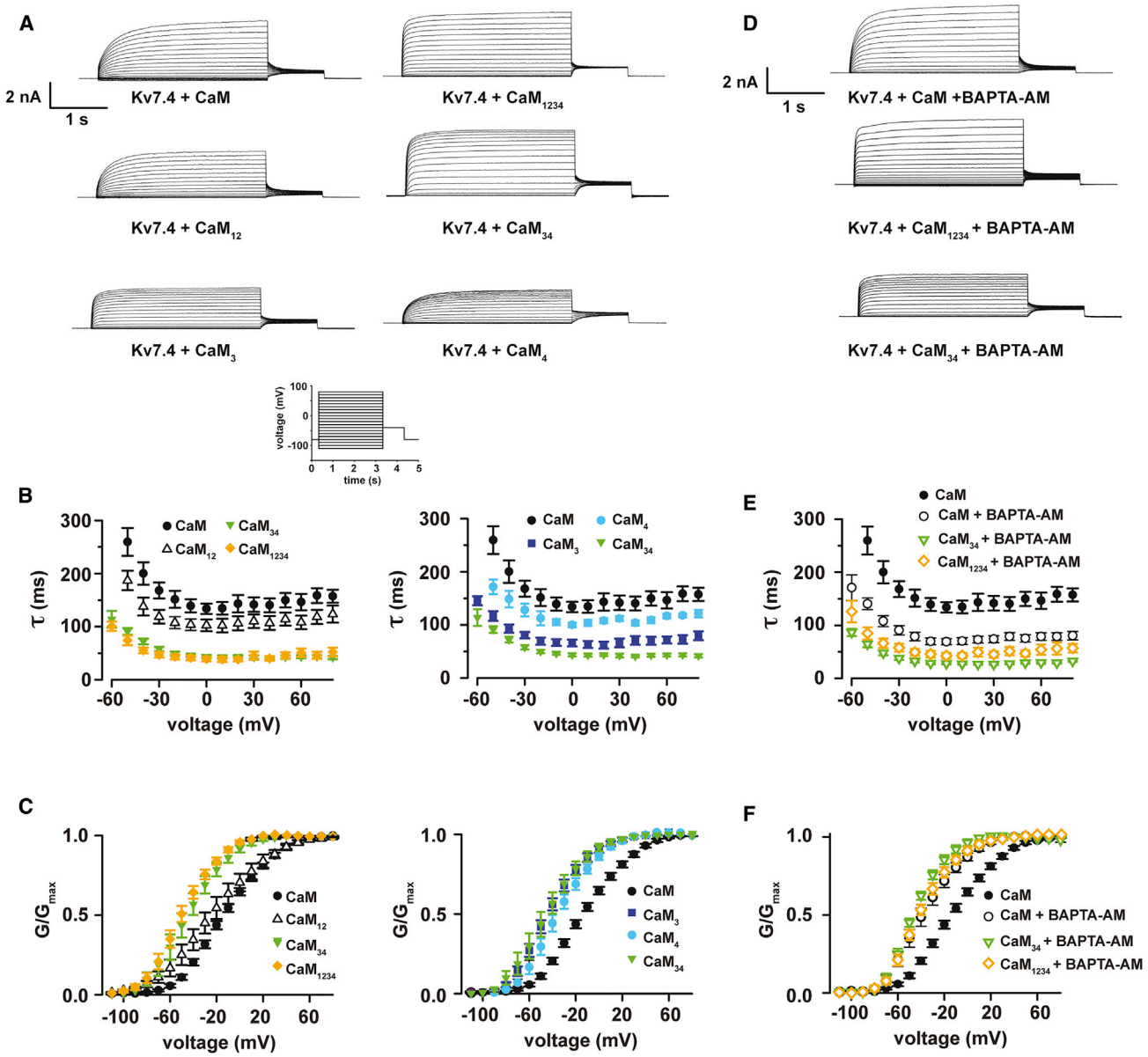

Figure 6. Ca^{2+}-CaM C-Lobe Switch Controls Kv7.4 Activation

(A) Exemplar traces from cells co-expressing Kv7.4 with CaM or indicated CaM mutants.

(B) Average time constant for the fast component of Kv7.4 activation for CaM combinations: CaM (black circles), CaM_{12} (open triangles), CaM_{34} (green triangles), CaM_{1234} (orange diamonds), CaM_3 (dark blue squares), CaM_4 (light blue circles). n = 8–12.

(C) Voltage-dependent activation curves for Kv7.4:CaM combinations. Symbols are as in (B).

(D) Exemplar traces from cells co-expressing Kv7.4 with CaM or indicated CaM mutants and pre-treated with 10 μM BAPTA-AM.

(E) Average time constant for the fast component of Kv7.4 activation for CaM/BAPTA-AM (open black circles) CaM_{34}/BAPTA-AM (open green triangles), CaM_{1234}/BAPTA-AM (open orange diamonds). n = 5–12.

(F) Voltage-dependent activation curves for Kv7.4:CaM combinations.

Error bars are SEM. Symbols are as in (E). Values for (C) and (F) are found in Table S4. See also Figures S9 and S10 and Table S4.

CaM_{12} and CaM_{1234} into Kv7.1/KCNE-expressing cells that did not affect $V_{1/2}$ but suppressed current density (Sachyani et al., 2014), and the lack of effect of BAPTA on Kv7.1 activation (Tobelaim et al., 2017a). These dissimilarities may result from experimental differences regarding the impact of diluting the cytosol by using the whole-cell configuration (Sachyani et al., 2014; Tobelaim et al., 2017a) instead of the perforated-patch configuration used here, or issues regarding how CaM is incorporated into the channel complex. Given that CaM is essential for Kv7.1 assembly and trafficking (Ghosh et al., 2006; Shamgar

et al., 2006), it is unclear whether efficient exchange can happen post assembly. Our results establish a central role for CaM C-lobe in effecting Kv7 calcium-dependent modulation that is independent of the coupling direction and suggest a unified mechanism for how CaM controls Kv7 activity.

Apo/CaM:Kv7.4 Interactions Control Channel Trafficking

Because we expect that the Apo/CaM clamp should represent the channel basal state, we made a set of structure-based mutations to probe the effects of interfering with Apo/CaM:Kv7.4 AB domain interactions. We mutated hydrophobic residues buried by each CaM lobe to either alanine or aspartate to disrupt Apo/C-lobe:A helix (I346A and I346D) and Apo/N-lobe:B helix interactions (S536A/L540A and S536D/L540D). Pull-down experiments using a fusion protein of the C-terminal tail construct used in the SAXS experiments, HMT-Kv7.4 AD (Δ368–492), revealed that all of these changes, except for S536A/L540A substantially impaired Apo/CaM binding (Figure 7A). Notably, all of these mutations, except for S536A/L540A, affected function and those that were most disruptive to binding (I346A, I346D, and S536D/L540D) resulted in either a substantial reduction (I346A) or complete loss (I346D and S536D/L540D) of Kv7.4 currents (Figures 7B and 7C). Further, even though the channel protein was made for each of the mutants, surface biotinylation experiments using an HA-tagged Kv7.4 demonstrated that the loss of interactions with Apo/CaM observed in the biochemical experiments (Figure 7A) were correlated with a strong negative impact on channel plasma membrane expression (Figure 7D). The I346A mutant had some surface expression and low current density that could be improved by providing CaM in excess. Nevertheless, the ability of CaM to rescue this mutant was far from complete, corroborating the CaM binding deficit observed in Apo/C-lobe binding site disruption (Figures 7A–7C). Together, these data support the idea that Apo/CaM:Kv7.4 interactions are essential for proper trafficking and are reminiscent of effects reported for mutations that disrupt the interaction between CaM and Kv7.1 (Ghosh et al., 2006; Shamgar et al., 2006), Kv7.2 (Etxeberria et al., 2008), and the Kv7.2/Kv7.3 heteromeric channel (Liu and Devaux, 2014). Hence, Apo/CaM interactions are essential for the formation of functional plasma membrane channels and set the stage for the regulation by the C-lobe-mediated calcium-dependent switch.

DISCUSSION

Intracellular calcium signals sensed by CaM exert strong control over Kv7 function (Gamper and Shapiro, 2003; Ghosh et al., 2006; Shamgar et al., 2006; Wen and Levitan, 2002; Yus-Najera et al., 2002). Although CaM is a well-established Kv7 co-factor (Gamper et al., 2005; Gamper and Shapiro, 2003; Ghosh et al., 2006; Shamgar et al., 2006), the roles of the various possible calcium-bound CaM forms have been unclear. Previous studies have shown that Apo/CaM binding requires the presence of the A and B segments of the Kv7 CTD (Wen and Levitan, 2002; Xu et al., 2013; Yus-Najera et al., 2002). The structure presented here of the Apo/CaM:Kv7.4 AB domain complex provides a clear rationale for this observation as the Apo/CaM form embraces an antiparallel pair of A and B helices (Figure 1). The importance of this interaction is further supported by the observations that disruptions in Apo/CaM binding impair plasma membrane expression (Figure 7) and agrees with previous observations made for Kv7.1 (Ghosh et al., 2006; Shamgar et al., 2006), Kv7.2 (Etxeberria et al., 2008), and the Kv7.2/Kv7.3 heteromeric channel (Liu and Devaux, 2014). Together, these observations support the role of CaM as Kv7 auxiliary subunit (Etxeberria et al., 2008; Gamper et al., 2005; Gamper and Shapiro, 2003; Ghosh et al., 2006; Levitan, 2006; Shamgar et al., 2006; Wen and Levitan, 2002; Yus-Najera et al., 2002).

Calcium-dependent conformational changes are at the heart of CaM function (Clapham, 2007; Hoeflich and Ikura, 2002), and CaM calcium-binding properties are dramatically shaped by context-dependent interactions with individual targets (Evans and Shea, 2009; Findeisen et al., 2013; Schumacher et al., 2004; Xia and Storm, 2005; Zhang et al., 2012). Our data reveal key features regarding how CaM:Kv7 AB domain interactions tune the individual Apo/CaM lobe properties, each of which have different conformations despite both engaging a helical partner. The open conformation of Apo/N-lobe bound to the B helix is essentially identical to the B helix-bound Ca^{2+}/N-lobe, sparing EF1 and EF2 calcium ligand differences, and adopts a mode of target recognition that is completely different from other Apo/N-lobe: target complex structures (Houdusse et al., 2006; Lu et al., 2015). In line with this largely pre-organized Ca^{2+} binding site, Ca^{2+} soaking experiments show that the N-lobe becomes preferentially loaded with Ca^{2+} without affecting how the N-lobe engages the Kv7.4 B helix. This pre-organization of the EF1 and EF2 calcium binding sites results in a >50-fold (>3 kcal mol^{-1}) Ca^{2+}-dependent increase in the affinity of the N-lobe:B helix interaction. This enhanced N-lobe calcium affinity may explain why other studies have not obtained structures in which the N-lobe is in the Apo state (Sachyani et al., 2014). Hence, even though Ca^{2+} binding does not shape the N-lobe:B helix structure, pre-organizing the N-lobe into a Ca^{2+}-bound-like open conformation by the Apo/CaM:Kv7 AB clamp allows Ca^{2+} to provide the critical stabilization of the N-lobe/B helix interaction required for Kv7 modulation by CaM.

By contrast, the Apo/C-lobe binds to an IQ motif in the A helix in a semi-open conformation that is essentially identical to that seen in the Apo/C-lobe:Myosin IQ domain complex (Houdusse et al., 2006) (Figures 2E and 2F) and other Apo/C-lobe:IQ domain complexes (Chagot and Chazin, 2011; Feldkamp et al., 2011; Wang et al., 2012), emphasizing the important roles of IQ motifs as sites for Apo/CaM anchoring (Bähler and Rhoads, 2002; Rhoads and Friedberg, 1997; Tidow and Nissen, 2013). The clear differences between this conformation and the open Ca^{2+}/C-lobe conformation in the Ca^{2+}/CaM:Kv7.4 B helix complex (Xu et al., 2013) indicates that the Apo/C-lobe is poised to respond to calcium signals through a calcium-induced conformational change. This idea is supported by SAXS experiments on Kv7 C-terminal constructs (Figure 5) that reveal structural changes consistent with C-lobe calcium-dependent conformational changes. The Apo/CaM:Kv7.4 AD and Ca^{2+}/CaM:Kv7.4 AD complexes adopt different conformations in solution. Notably, Ca^{2+}/CaM:Kv7.4 AD has a less compact structure than Apo/CaM:Kv7.4 AD or Ca^{2+}/CaM:Kv7.4 BD, both of which

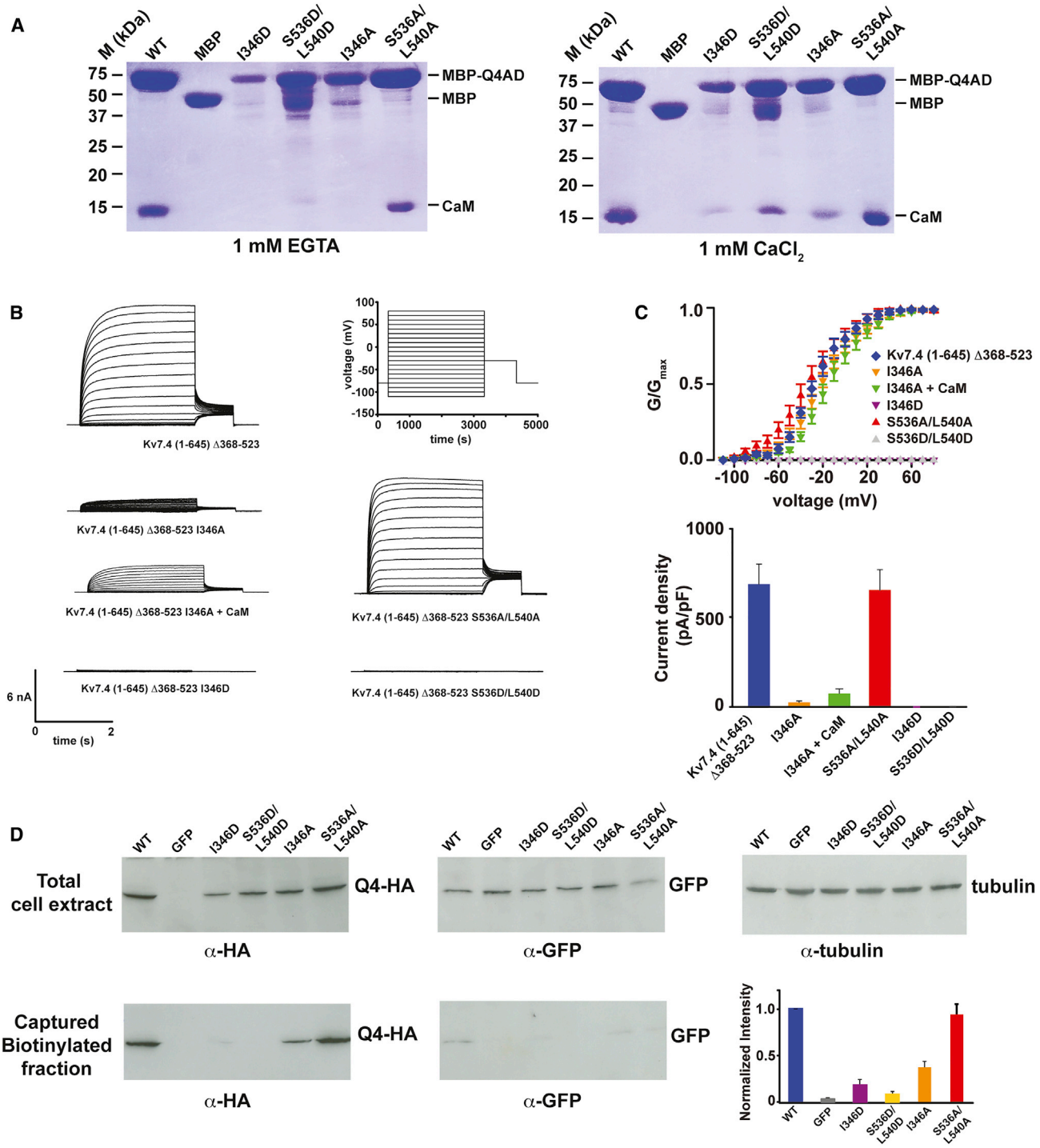

Figure 7. Loss of Apo/CaM Binding Suppresses Channel Function and Cell-Surface Expression

(A) SDS-PAGE analysis of a Apo/CaM:Kv7.4 AD (left) and Ca^{2+}/CaM:Kv7.4 AD (right) pull-downs for wild-type (WT) and indicated mutants.

(B) Exemplar Kv7.4 potassium currents evoked using the indicated protocol.

(C) Voltage-dependent activation (upper panel) and current density at +80 mV (lower panel) for the indicated Kv7.4 channels: Kv7.4 (blue diamonds), I346A (orange inverted triangles), I346A + CaM (green inverted triangles), I346D (purple inverted triangles), S536A/L540A (red triangles), S536D/L540D (gray triangles), n = 6–50.

(D) Exemplar western blots of total lysate and surface biotinylated fractions for Kv7.4 1–645 Δ368–523 (WT) and indicated mutants using the specified antibodies. Lower-right panel shows quantified intensities in which the α-HA intensities in the captured biotinylated fraction are normalized by the α-tubulin intensities in the total cell extract intensities (n = 4).

Error bars are SEM. See also Table S4 for values for (C).

are similarly compact, even though they have different length CTDs. These features together with the increased flexibility in the Ca^{2+}/CaM:Kv7.4 AD complex are consistent with a calcium-dependent disruption of the C-lobe:A helix interaction (Figure 5). Such a situation maximally involves a complete loss of half of the interaction made by Apo/CaM clamp conformation. Because the Apo/N-lobe:B helix interaction is weak (Figure 3), the calcium-dependent binding affinity change for the N-lobe:B helix interaction would compensate the affinity loss resulting from the conformational change induced by disruption of the Apo/C-lobe:A helix interactions and Apo/CaM clamp. This affinity enhancement would then allow CaM to remain anchored to the Kv7.4 tail. Although similar SAXS comparisons of calcium-bound and apo states using engineered Kv7.3/Kv7.2 AB domain chimera were not possible due to aggregation problems in the presence of calcium (Strulovich et al., 2016), given the highly conserved nature of the Kv7 AB domain, we expect that other Kv7 isoforms will have similar calcium-dependent structural changes in the CaM:AB domain modulatory element.

In agreement with the structural data, our functional studies strongly support a central role for the C-lobe in Kv7 calcium-dependent modulation in both Kv7.4 and Kv7.1, even though the impacts on channel function differ. C-lobe calcium-dependent modulation of Kv7.4 affects channel activation kinetics and voltage-dependent opening (Figure 6). The ability of the CaM C-lobe mutant CaM_{34} to phenocopy CaM_{1234} and the observation that BAPTA causes similar changes in activation kinetics and voltage-dependent opening to Kv7.4 expressed with wild-type CaM but not CaM_{1234} or CaM_{34} indicate that Apo/C-lobe facilitates both processes and support a model for Kv7.4 modulation in which the Apo/CaM clamp facilitates channel activation. These observations are in agreement with the ability of CaM_{1234} to increase channel open probability (Sihn et al., 2016). Further, our studies with Kv7.5 (Figure S9D), together with prior studies of the effects of CaM_{1234} on Kv7.2 and Kv7.3, demonstrate a unified role for Apo/CaM in facilitating the activation of the neuronal Kv7.2–Kv7.5 isoforms. Interestingly, we find a similar C-lobe dependence for Kv7.1 modulation (Figures S9E–S9G; Table S4), even though the Apo/CaM form acts as an inhibitor rather than a facilitator of voltage-dependent activation. These results point to a model in which disruption of C-lobe:Kv7 interactions facilitates Kv7.1 activation and opening. The observation that a CaM C-lobe disease mutation affects Kv7.1 function corroborates the importance of the C-lobe in gating (Sun and MacKinnon, 2017). In both Kv7.4 and Kv7.1, we find that CaM_{12} is not a perfect substitute for wild-type CaM, a result that may reflect a loss of the proposed role for Ca^{2+}/N-lobe as an anchor. The observation that the CaM EF hand mutant effects are phenocopied when cellular calcium levels are decreased using BAPTA suggests that, under resting conditions, there may be some tonic occupation of the EF hands by calcium and would be in line with the idea that the various structures having differently bound lobes reflect intermediates between the fully Apo/CaM state and the actuated Ca^{2+}-bound conformation.

The clear role of the C-lobe in controlling Kv7 function contrasts with previous studies suggesting that the CaM N-lobe, not the C-lobe, mediates the Kv7.4 calcium sensitivity (Gamper et al., 2005). The discrepancy with the previous report may arise from different experimental approaches regarding calcium manipulations and how mutant CaM expression was verified. We tested cells under resting calcium conditions that express the CaM variants supplied using a pIRES-GFP vector ensuring delivery of the mutant CaMs to the tested cells, an approach not used in the prior study (Gamper et al., 2005). Further, the prior work used a calcium ionophore combined with different extracellular Ca^{2+} concentrations to change intracellular Ca^{2+} concentration and did not compare uniform calcium exposures to the tested mutants. Consequently, changes in current amplitude observed by Gamper and colleagues could be indirect effects from large calcium changes rather than CaM-dependent modulation. Notably, this previous study also failed to find CaM-dependent modulation of Kv7.1 and Kv7.3, both of which were later shown to have CaM-dependent modulation (Gomis-Perez et al., 2017; Sachyani et al., 2014; Tobelaim et al., 2017b), a result for Kv7.1 that is confirmed by our studies (Figures S9E–S9G). The excellent correlation of our structural data with our functional studies, done under comparable calcium levels for the various CaM versions (Figure S9B) and borne out in two different Kv7s, strongly supports the central role of the C-lobe as the driver in controlling Kv7 responses to calcium.

Our studies of individual EF hand mutants show that EF3 is the key element of the C-lobe-mediated channel modulation (Figure 6). Structural studies of a CaM:Kv7.1 channel complex indicate that Apo/EF3 interacts with the S2–S3 linker of the Kv7 VSDs (Sun and MacKinnon, 2017). Indeed, structural comparison with the Apo/CaM:Kv7.4 AB domain complex shows that despite the differences in EF4, which is ion bound in the CaM:Kv7.1 complex but empty in the Apo/CaM Kv7.4 complex, both EF3s have similar conformations (Figure 8A). Hence, calcium binding to EF3 would produce a substantial conformational change in the C-lobe as evident from the comparison with the Ca^{2+}/C-lobe structure (Figure 8A). This conformational change would perturb the interaction with the A helix and interactions with the VSD mediated by the S2/S3 loop. Thus, in addition to effects on the pore domain mediated by the A helix, there may also be an untethering of the membrane proximal modulatory domain from the VSD that affects VSD motions and activation. The importance of the Apo/CaM interaction for channel function and cell-surface trafficking underscores the role of the clamped conformation in setting the basal state of the channel.

Our structural observations and functional results demonstrate that CaM C-lobe is the key moving part underling calcium-dependent Kv7 modulation by CaM and lead us to propose the following unified Kv7 modulation model (Figure 8B) centered on the importance of the Apo/CaM clamp configuration. This clamp conformation, common to all Kv7 isoforms, promotes the opening of Kv7.2–Kv7.5 channels but opposes Kv7.1 activation. Loading of the CaM C-lobe with calcium drives the C-lobe from the semi-open to an open conformation and releases the interactions with the A helix. In the most extreme case, this change would lead to an increased A helix disorder as observed in our SAXS studies and Ca^{2+}/C-lobe binding to the B helix as in the Ca^{2+}/CaM:Kv7.4 B helix complex (Movie S1). The increased affinity of the Ca^{2+}/N-lobe for the B helix compensates for the disruption of C/lobe:A helix interactions anchoring CaM on the

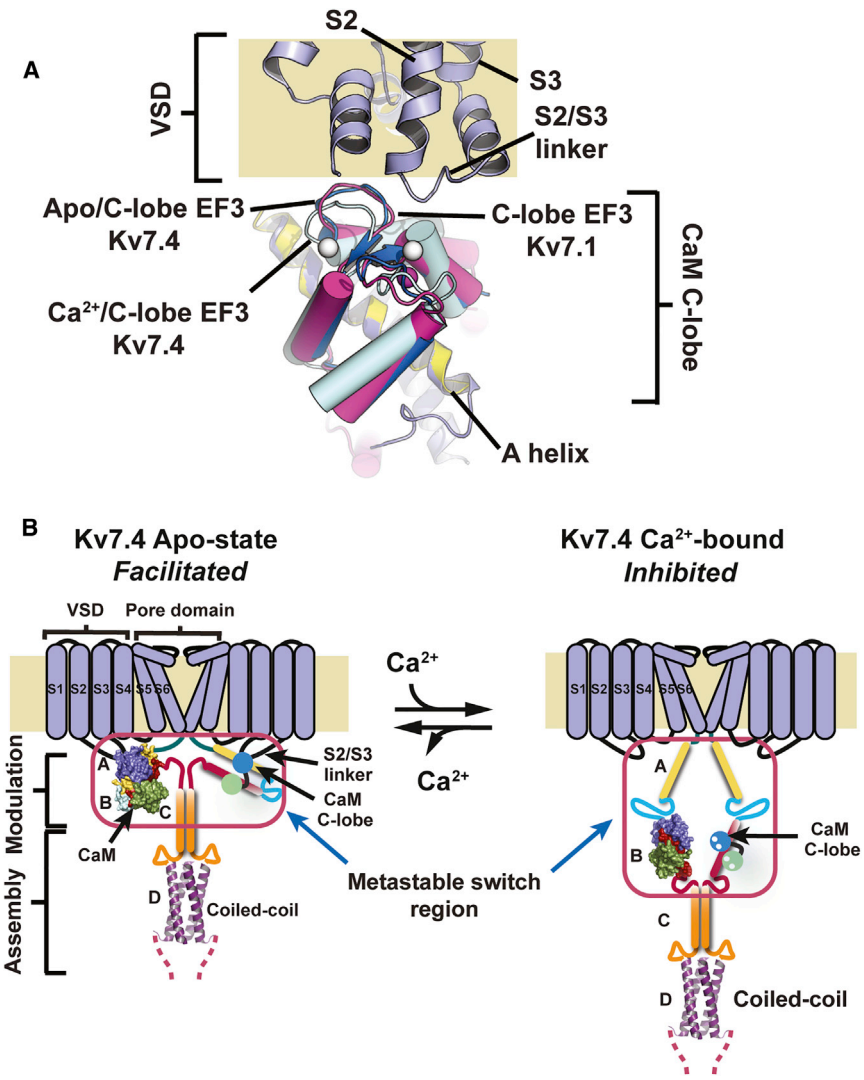

Figure 8. CaM C-Lobe Switch Controls Kv7 Function

(A) Structural comparison of CaM C-lobes from the CaM:Kv7.1 complex (5VMS) (magenta) (Sun and MacKinnon, 2017), Apo/CaM:K_V7.4: complex (marine), and Ca^{2+}/CaM (cyan) (Xu et al., 2013) (4GOW). A single Kv7.1 subunit is shown (slate) having key voltage sensor domain (VSD) elements labeled. Kv7.4 A helix (yellow) is shown superposed on the Kv7.1 A helix (slate). Calcium ions (spheres) from Ca^{2+}/CaM (white) and CaM:K_V7.1 (magenta) are shown.

(B) Model for Kv7.4 modulation by a CaM C-lobe switch. Metastable switch region resides between the pore domain and coiled-coil assembly domain. Apo/CaM and Ca^{2+}/CaM:B helix-bound states are shown. A helix structure changes are not diagramed. Two of four channel subunits are shown. VSD, pore domain, and elements involved in modulation and assembly are indicated for the left panel. For Kv7.1, the model is the same except that the Apo/CaM state is inhibited and the Ca^{2+}/CaM state is facilitated.

See also Figure S11.

channel as the C-lobe switch is thrown. Hence, while the C-lobe constitutes the moving part, the N-lobe remains in place on the B helix in both Apo- and Ca^{2+}-bound forms. This model is supported by our observation that calcium soaks of the Apo/CaM form leads to preferential N-lobe loading (Figures 3 and S6). Given the potential for Apo/C-lobe:S2/S3 linker interactions (Sun and MacKinnon, 2017), and the fact that it is possible to obtain clamped conformations in the presence of calcium (Sachyani et al., 2014; Strulovich et al., 2016), interactions with other channel elements or the membrane may constrain the extent of such conformational changes in the full-length channel. Additionally, there is likely to be important interplay of CaM with other Kv7 regulatory factors, especially the signaling lipid phosphytidylionsitol-4,5-bisphosphate (PIP_2), as CaM:Kv7 interactions occur near regions implicated in PIP_2 modulation (Gamper and Shapiro, 2007; Gomis-Perez et al., 2017; Hernandez et al., 2009; Li et al., 2005; Logothetis et al., 2015; Tobelaim et al., 2017a, 2017b; Zaydman and Cui, 2014; Zaydman et al., 2013). Taken together, our studies suggest a unified framework for understanding how CaM affects Kv7 function centered on the shared CaM clamp configuration. Calcium binding to the C-lobe perturbs interactions with the A helix that lead to channel inhibition in non-Kv7.1 isoforms and channel facilitation for Kv7.1. Notably, the S2/S3 linker has only four conserved residues among all isoforms and a number of the positions that face the C-lobe differ between Kv7.1 and the neuronal isoforms Kv7.2–Kv7.5 (positions 2, 4, and 6) (Figure S11). Such differences may contribute to the opposite outcomes from releasing the C-lobe switch. Future studies of full-length Kv7s in both high and low calcium conditions and in membrane environments, as well as studies of the impact of the S2/S3 loop differences on Kv7 modulation should enlighten the details of this process and the molecular determinants governing the opposite coupling observed for CaM effects on Kv7.1 and Kv7.2–Kv7.5.

The Kv7 channel architecture in which the pore domain is followed by long cytoplasmic domain bearing a membrane proximal regulatory region followed by a coiled-coil assembly domain is one of the most general voltage-gated ion channel (VGIC) body plans, occurring in Kv7 (Howard et al., 2007; Jenke et al., 2003; Wiener et al., 2008), TRPM (Erler et al., 2006; Mei et al., 2006; Tsuruda et al., 2006), TRPA1 (Paulsen et al., 2015), TRPP (Ćelić et al., 2012; Qian et al., 1997; Tsiokas et al., 1997; Yu et al., 2009, 2012), and $BacNa_V$ (Arrigoni et al., 2016; Payandeh and Minor, 2015; Shaya et al., 2014) channels. The observations here regarding the key role of conformational changes in the membrane proximal domain in Kv7 channel modulation and our previous work establishing the importance of the $BacNa_V$

membrane proximal region in thermal sensing (Arrigoni et al., 2016) suggest that a key feature of this general architecture is to enable the membrane proximal region, which is framed by the channel pore and the coiled coil, to adopt metastable conformations that can be switched by various types of signals to control channel function. Moreover, the observation that there can be direct contacts between the modulatory domain and the VSDs highlights the potential for direct impacts of cytoplasmic domains on VSD action as suggested by studies on other VGIC family members (Lee and MacKinnon, 2017; Whicher and MacKinnon, 2016).

STAR★METHODS

Detailed methods are provided in the online version of this paper and include the following:

- KEY RESOURCES TABLE
- CONTACT FOR REAGENT AND RESOURCE SHARING
- EXPERIMENTAL MODEL AND SUBJECT DETAILS
  - Cell Culture
- METHOD DETAILS
  - Protein expression and purification
  - Isothermal titration calorimetry (ITC)
  - Crystallization, data collection, structure determination, and refinement
  - Small angle X-ray scattering (SAXS)
  - Pull-down experiments
  - Electrophysiology
  - Calcium level measurements by flow cytometry
  - Biotinylation
- QUANTIFICATION AND STATISTICAL ANALYSIS
  - Calcium level measurements by flow cytometry
  - Biotinylation
- DATA AND SOFTWARE AVAILABILITY

SUPPLEMENTAL INFORMATION

Supplemental Information includes 11 figures, four tables, and one movie and can be found with this article online at https://doi.org/10.1016/j.neuron.2018.01.035.

A video abstract is available at https://doi.org/10.1016/j.neuron.2018.01.035#mmc4.

ACKNOWLEDGMENTS

We thank S.J. Kim for help with SAXS analysis, J. Kung and N. Michael for help with FACS experiments, and C. Arrigoni, K. Brejc, L. Jan, M. Lolicato, A. Moroni, and G. Thiel for comments on the manuscript. This work was supported by NIH grants NIH-NIDCD R01-DC007664 to D.L.M., NIH-HLBI T32HL007731 and NIH-NIGMS F32GM 109537 to A.C., and a Marcel Bleustein-Blanchet Foundation fellowship to F.A.-A.

AUTHOR CONTRIBUTIONS

A.C., F.A.-A., and D.L.M. conceived the study and designed the experiments. A.C. and R.E.G. expressed and purified the proteins. A.C. crystallized the proteins and determined the structures, performed ITC and biochemistry experiments, and analyzed the data. F.A.-A. and N.D.R. performed electrophysiology experiments. F.A.-A. analyzed the electrophysiology data. A.C. and F.A.-A performed molecular biology experiments. A.C. and G.L.H. performed the SAXS experiments and analyzed the data. F.A.-A. performed flow cytometry experiments and analyzed the data. D.L.M. analyzed data and provided guidance and support. A.C., F.A.-A., and D.L.M. wrote the paper.

DECLARATION OF INTERESTS

The authors declare no competing interests.

Received: October 10, 2017
Revised: December 7, 2017
Accepted: January 12, 2018
Published: February 8, 2018

REFERENCES

Adams, P.D., Afonine, P.V., Bunkóczi, G., Chen, V.B., Davis, I.W., Echols, N., Headd, J.J., Hung, L.W., Kapral, G.J., Grosse-Kunstleve, R.W., et al. (2010). PHENIX: A comprehensive Python-based system for macromolecular structure solution. Acta Crystallogr. D Biol. Crystallogr. *66*, 213–221.

Alaimo, A., Alberdi, A., Gomis-Perez, C., Fernández-Orth, J., Bernardo-Seisdedos, G., Malo, C., Millet, O., Areso, P., and Villarroel, A. (2014). Pivoting between calmodulin lobes triggered by calcium in the Kv7.2/calmodulin complex. PLoS ONE *9*, e86711.

Arrigoni, C., Rohaim, A., Shaya, D., Findeisen, F., Stein, R.A., Nurva, S.R., Mishra, S., Mchaourab, H.S., and Minor, D.L., Jr. (2016). Unfolding of a temperature-sensitive domain controls voltage-gated channel activation. Cell *164*, 922–936.

Bähler, M., and Rhoads, A. (2002). Calmodulin signaling via the IQ motif. FEBS Lett. *513*, 107–113.

Bal, M., Zaika, O., Martin, P., and Shapiro, M.S. (2008). Calmodulin binding to M-type K+ channels assayed by TIRF/FRET in living cells. J. Physiol. *586*, 2307–2320.

Barhanin, J., Lesage, F., Guillemare, E., Fink, M., Lazdunski, M., and Romey, G. (1996). K(V)LQT1 and IsK (minK) proteins associate to form the I(Ks) cardiac potassium current. Nature *384*, 78–80.

Ćelić, A.S., Petri, E.T., Benbow, J., Hodsdon, M.E., Ehrlich, B.E., and Boggon, T.J. (2012). Calcium-induced conformational changes in C-terminal tail of polycystin-2 are necessary for channel gating. J. Biol. Chem. *287*, 17232–17240.

Chagot, B., and Chazin, W.J. (2011). Solution NMR structure of Apo-calmodulin in complex with the IQ motif of human cardiac sodium channel NaV1.5. J. Mol. Biol. *406*, 106–119.

Chen, V.B., Arendall, W.B., 3rd, Headd, J.J., Keedy, D.A., Immormino, R.M., Kapral, G.J., Murray, L.W., Richardson, J.S., and Richardson, D.C. (2010). MolProbity: All-atom structure validation for macromolecular crystallography. Acta Crystallogr. D Biol. Crystallogr. *66*, 12–21.

Clapham, D.E. (2007). Calcium signaling. Cell *131*, 1047–1058.

Delmas, P., and Brown, D.A. (2005). Pathways modulating neural KCNQ/M (Kv7) potassium channels. Nat. Rev. Neurosci. *6*, 850–862.

Edelhoch, H. (1967). Spectroscopic determination of tryptophan and tyrosine in proteins. Biochemistry *6*, 1948–1954.

Emsley, P., and Cowtan, K. (2004). Coot: Model-building tools for molecular graphics. Acta Crystallogr. D Biol. Crystallogr. *60*, 2126–2132.

Erler, I., Al-Ansary, D.M., Wissenbach, U., Wagner, T.F., Flockerzi, V., and Niemeyer, B.A. (2006). Trafficking and assembly of the cold-sensitive TRPM8 channel. J. Biol. Chem. *281*, 38396–38404.

Etxeberria, A., Aivar, P., Rodriguez-Alfaro, J.A., Alaimo, A., Villacé, P., Gómez-Posada, J.C., Areso, P., and Villarroel, A. (2008). Calmodulin regulates the trafficking of KCNQ2 potassium channels. FASEB J. *22*, 1135–1143.

Evans, T.I., and Shea, M.A. (2009). Energetics of calmodulin domain interactions with the calmodulin binding domain of CaMKII. Proteins *76*, 47–61.

Feldkamp, M.D., Yu, L., and Shea, M.A. (2011). Structural and energetic determinants of apo calmodulin binding to the IQ motif of the Na(V)1.2 voltage-dependent sodium channel. Structure *19*, 733–747.

Findeisen, F., Rumpf, C.H., and Minor, D.L., Jr. (2013). Apo states of calmodulin and CaBP1 control CaV1 voltage-gated calcium channel function through direct competition for the IQ domain. J. Mol. Biol. *425*, 3217–3234.

Fischer, H., Neto, M.D., Napolitano, H.B., Polikarpov, I., and Craievich, A.F. (2010). Determination of the molecular weight of proteins in solution from a single small-angle X-ray scattering measurement on a relative scale. J. Appl. Crystallogr. *43*, 101–109.

Forster, S., Apostol, L., and Bras, W. (2010). Scatter: Software for the analysis of nano- and mesoscale small-angle scattering. J. Appl. Crystallogr. *43*, 639–646.

Gamper, N., and Shapiro, M.S. (2003). Calmodulin mediates Ca2+-dependent modulation of M-type K+ channels. J. Gen. Physiol. *122*, 17–31.

Gamper, N., and Shapiro, M.S. (2007). Target-specific PIP(2) signalling: How might it work? J. Physiol. *582*, 967–975.

Gamper, N., Li, Y., and Shapiro, M.S. (2005). Structural requirements for differential sensitivity of KCNQ K+ channels to modulation by Ca2+/calmodulin. Mol. Biol. Cell *16*, 3538–3551.

Ghosh, S., Nunziato, D.A., and Pitt, G.S. (2006). KCNQ1 assembly and function is blocked by long-QT syndrome mutations that disrupt interaction with calmodulin. Circ. Res. *98*, 1048–1054.

Gomis-Perez, C., Soldovieri, M.V., Malo, C., Ambrosino, P., Taglialatela, M., Areso, P., and Villarroel, A. (2017). Differential regulation of PI(4,5)P2 sensitivity of Kv7.2 and Kv7.3 channels by calmodulin. Front. Mol. Neurosci. *10*, 117.

Grabarek, Z. (2011). Insights into modulation of calcium signaling by magnesium in calmodulin, troponin C and related EF-hand proteins. Biochim. Biophys. Acta *1813*, 913–921.

Gutman, G.A., Chandy, K.G., Adelman, J.P., Aiyar, J., Bayliss, D.A., Clapham, D.E., Covarriubias, M., Desir, G.V., Furuichi, K., Ganetzky, B., et al.; International Union of Pharmacology (2003). International Union of Pharmacology. XLI. Compendium of voltage-gated ion channels: Potassium channels. Pharmacol. Rev. *55*, 583–586.

Haitin, Y., and Attali, B. (2008). The C-terminus of Kv7 channels: A multifunctional module. J. Physiol. *586*, 1803–1810.

Haitin, Y., Wiener, R., Shaham, D., Peretz, A., Cohen, E.B., Shamgar, L., Pongs, O., Hirsch, J.A., and Attali, B. (2009). Intracellular domains interactions and gated motions of I(KS) potassium channel subunits. EMBO J. *28*, 1994–2005.

Hammel, M. (2012). Validation of macromolecular flexibility in solution by small-angle X-ray scattering (SAXS). Eur. Biophys. J. *41*, 789–799.

Hernandez, C.C., Zaika, O., Tolstykh, G.P., and Shapiro, M.S. (2008). Regulation of neural KCNQ channels: Signalling pathways, structural motifs and functional implications. J. Physiol. *586*, 1811–1821.

Hernandez, C.C., Falkenburger, B., and Shapiro, M.S. (2009). Affinity for phosphatidylinositol 4,5-bisphosphate determines muscarinic agonist sensitivity of Kv7 K+ channels. J. Gen. Physiol. *134*, 437–448.

Hoeflich, K.P., and Ikura, M. (2002). Calmodulin in action: Diversity in target recognition and activation mechanisms. Cell *108*, 739–742.

Horn, R., and Marty, A. (1988). Muscarinic activation of ionic currents measured by a new whole-cell recording method. J. Gen. Physiol. *92*, 145–159.

Houdusse, A., Gaucher, J.F., Krementsova, E., Mui, S., Trybus, K.M., and Cohen, C. (2006). Crystal structure of apo-calmodulin bound to the first two IQ motifs of myosin V reveals essential recognition features. Proc. Natl. Acad. Sci. USA *103*, 19326–19331.

Howard, R.J., Clark, K.A., Holton, J.M., and Minor, D.L., Jr. (2007). Structural insight into KCNQ (Kv7) channel assembly and channelopathy. Neuron *53*, 663–675.

Jenke, M., Sánchez, A., Monje, F., Stühmer, W., Weseloh, R.M., and Pardo, L.A. (2003). C-terminal domains implicated in the functional surface expression of potassium channels. EMBO J. *22*, 395–403.

Jentsch, T.J. (2000). Neuronal KCNQ potassium channels: Physiology and role in disease. Nat. Rev. Neurosci. *1*, 21–30.

Jespersen, T., Grunnet, M., and Olesen, S.P. (2005). The KCNQ1 potassium channel: From gene to physiological function. Physiology (Bethesda) *20*, 408–416.

Kabsch, W. (2010). Xds. Acta Crystallogr. D Biol. Crystallogr. *66*, 125–132.

Keen, J.E., Khawaled, R., Farrens, D.L., Neelands, T., Rivard, A., Bond, C.T., Janowsky, A., Fakler, B., Adelman, J.P., and Maylie, J. (1999). Domains responsible for constitutive and Ca(2+)-dependent interactions between calmodulin and small conductance Ca(2+)-activated potassium channels. J. Neurosci. *19*, 8830–8838.

Konarev, P.V., Volkov, V.V., Sokolova, A.V., Koch, M.H.J., and Svergun, D.I. (2003). PRIMUS: A Windows PC-based system for small-angle scattering data analysis. J. Appl. Crystallogr. *36*, 1277–1282.

Krissinel, E., and Henrick, K. (2007). Inference of macromolecular assemblies from crystalline state. J. Mol. Biol. *372*, 774–797.

Lee, C.H., and MacKinnon, R. (2017). Structures of the human HCN1 hyperpolarization-activated channel. Cell *168*, 111–120.

Levitan, I.B. (2006). Signaling protein complexes associated with neuronal ion channels. Nat. Neurosci. *9*, 305–310.

Li, Y., Gamper, N., Hilgemann, D.W., and Shapiro, M.S. (2005). Regulation of Kv7 (KCNQ) K+ channel open probability by phosphatidylinositol 4,5-bisphosphate. J. Neurosci. *25*, 9825–9835.

Linse, S., Helmersson, A., and Forsén, S. (1991). Calcium binding to calmodulin and its globular domains. J. Biol. Chem. *266*, 8050–8054.

Liu, W., and Devaux, J.J. (2014). Calmodulin orchestrates the heteromeric assembly and the trafficking of KCNQ2/3 (Kv7.2/3) channels in neurons. Mol. Cell. Neurosci. *58*, 40–52.

Logothetis, D.E., Petrou, V.I., Zhang, M., Mahajan, R., Meng, X.Y., Adney, S.K., Cui, M., and Baki, L. (2015). Phosphoinositide control of membrane protein function: A frontier led by studies on ion channels. Annu. Rev. Physiol. *77*, 81–104.

Lu, Q., Li, J., Ye, F., and Zhang, M. (2015). Structure of myosin-1c tail bound to calmodulin provides insights into calcium-mediated conformational coupling. Nat. Struct. Mol. Biol. *22*, 81–88.

Maljevic, S., Wuttke, T.V., Seebohm, G., and Lerche, H. (2010). KV7 channelopathies. Pflugers Arch. *460*, 277–288.

Meador, W.E., Means, A.R., and Quiocho, F.A. (1992). Target enzyme recognition by calmodulin: 2.4 A structure of a calmodulin-peptide complex. Science *257*, 1251–1255.

Mei, Z.Z., Xia, R., Beech, D.J., and Jiang, L.H. (2006). Intracellular coiled-coil domain engaged in subunit interaction and assembly of melastatin-related transient receptor potential channel 2. J. Biol. Chem. *281*, 38748–38756.

O'Neil, K.T., and DeGrado, W.F. (1990). A thermodynamic scale for the helix-forming tendencies of the commonly occurring amino acids. Science *250*, 646–651.

Otwinowski, Z., and Minor, W. (1997). Processing of X-ray diffraction data collected in oscillation mode. Methods Enzymol. *276*, 307–326.

Paulsen, C.E., Armache, J.P., Gao, Y., Cheng, Y., and Julius, D. (2015). Structure of the TRPA1 ion channel suggests regulatory mechanisms. Nature *520*, 511–517.

Payandeh, J., and Minor, D.L., Jr. (2015). Bacterial voltage-gated sodium channels (BacNa(V)s) from the soil, sea, and salt lakes enlighten molecular mechanisms of electrical signaling and pharmacology in the brain and heart. J. Mol. Biol. *427*, 3–30.

Qian, F., Germino, F.J., Cai, Y., Zhang, X., Somlo, S., and Germino, G.G. (1997). PKD1 interacts with PKD2 through a probable coiled-coil domain. Nat. Genet. *16*, 179–183.

Rae, J., Cooper, K., Gates, P., and Watsky, M. (1991). Low access resistance perforated patch recordings using amphotericin B. J. Neurosci. Methods *37*, 15–26.

Rambo, R.P., and Tainer, J.A. (2011). Characterizing flexible and intrinsically unstructured biological macromolecules by SAS using the Porod-Debye law. Biopolymers *95*, 559–571.

Rhoads, A.R., and Friedberg, F. (1997). Sequence motifs for calmodulin recognition. FASEB J. *11*, 331–340.

Sachyani, D., Dvir, M., Strulovich, R., Tria, G., Tobelaim, W., Peretz, A., Pongs, O., Svergun, D., Attali, B., and Hirsch, J.A. (2014). Structural basis of a Kv7.1 potassium channel gating module: Studies of the intracellular c-terminal domain in complex with calmodulin. Structure *22*, 1582–1594.

Sanguinetti, M.C., Curran, M.E., Zou, A., Shen, J., Spector, P.S., Atkinson, D.L., and Keating, M.T. (1996). Coassembly of $K_{(V)}$LQT1 and minK (IsK) proteins to form cardiac $I_{(Ks)}$ potassium channel. Nature *384*, 80–83.

Schneider, C.A., Rasband, W.S., and Eliceiri, K.W. (2012). NIH Image to ImageJ: 25 years of image analysis. Nat. Methods *9*, 671–675.

Schumacher, M.A., Crum, M., and Miller, M.C. (2004). Crystal structures of apocalmodulin and an apocalmodulin/SK potassium channel gating domain complex. Structure *12*, 849–860.

Shamgar, L., Ma, L., Schmitt, N., Haitin, Y., Peretz, A., Wiener, R., Hirsch, J., Pongs, O., and Attali, B. (2006). Calmodulin is essential for cardiac IKS channel gating and assembly: Impaired function in long-QT mutations. Circ. Res. *98*, 1055–1063.

Shaya, D., Findeisen, F., Abderemane-Ali, F., Arrigoni, C., Wong, S., Nurva, S.R., Loussouarn, G., and Minor, D.L., Jr. (2014). Structure of a prokaryotic sodium channel pore reveals essential gating elements and an outer ion binding site common to eukaryotic channels. J. Mol. Biol. *426*, 467–483.

Sihn, C.R., Kim, H.J., Woltz, R.L., Yarov-Yarovoy, V., Yang, P.C., Xu, J., Clancy, C.E., Zhang, X.D., Chiamvimonvat, N., and Yamoah, E.N. (2016). Mechanisms of calmodulin regulation of different isoforms of Kv7.4 K+ channels. J. Biol. Chem. *291*, 2499–2509.

Soldovieri, M.V., Miceli, F., and Taglialatela, M. (2011). Driving with no brakes: Molecular pathophysiology of Kv7 potassium channels. Physiology (Bethesda) *26*, 365–376.

Strulovich, R., Tobelaim, W.S., Attali, B., and Hirsch, J.A. (2016). Structural insights into the M-channel proximal C-terminus/calmodulin complex. Biochemistry *55*, 5353–5365.

Sun, J., and MacKinnon, R. (2017). Cryo-EM structure of a KCNQ1/CaM complex reveals insights into congenital long QT syndrome. Cell *169*, 1042–1050.

Svergun, D.I. (1992). Determination of the regularization parameter in indirect-transform methods using perceptual criteria. J. Appl. Crystallogr. *25*, 495–503.

Tidow, H., and Nissen, P. (2013). Structural diversity of calmodulin binding to its target sites. FEBS J. *280*, 5551–5565.

Tobelaim, W.S., Dvir, M., Lebel, G., Cui, M., Buki, T., Peretz, A., Marom, M., Haitin, Y., Logothetis, D.E., Hirsch, J.A., and Attali, B. (2017a). Ca2+-Calmodulin and PIP2 interactions at the proximal C-terminus of Kv7 channels. Channels (Austin) *11*, 686–695.

Tobelaim, W.S., Dvir, M., Lebel, G., Cui, M., Buki, T., Peretz, A., Marom, M., Haitin, Y., Logothetis, D.E., Hirsch, J.A., and Attali, B. (2017b). Competition of calcified calmodulin N lobe and PIP2 to an LQT mutation site in Kv7.1 channel. Proc. Natl. Acad. Sci. USA *114*, E869–E878.

Tsiokas, L., Kim, E., Arnould, T., Sukhatme, V.P., and Walz, G. (1997). Homo- and heterodimeric interactions between the gene products of PKD1 and PKD2. Proc. Natl. Acad. Sci. USA *94*, 6965–6970.

Tsuruda, P.R., Julius, D., and Minor, D.L., Jr. (2006). Coiled coils direct assembly of a cold-activated TRP channel. Neuron *51*, 201–212.

Van Petegem, F., Chatelain, F.C., and Minor, D.L., Jr. (2005). Insights into voltage-gated calcium channel regulation from the structure of the CaV1.2 IQ domain-Ca2+/calmodulin complex. Nat. Struct. Mol. Biol. *12*, 1108–1115.

Wang, Q., Curran, M.E., Splawski, I., Burn, T.C., Millholland, J.M., VanRaay, T.J., Shen, J., Timothy, K.W., Vincent, G.M., de Jager, T., et al. (1996). Positional cloning of a novel potassium channel gene: KVLQT1 mutations cause cardiac arrhythmias. Nat. Genet. *12*, 17–23.

Wang, H.-S., Pan, Z., Shi, W., Brown, B.S., Wymore, R.S., Cohen, I.S., Dixon, J.E., and McKinnon, D. (1998). KCNQ2 and KCNQ3 potassium channel subunits: Molecular correlates of the M-channel. Science *282*, 1890–1893.

Wang, C., Chung, B.C., Yan, H., Lee, S.Y., and Pitt, G.S. (2012). Crystal structure of the ternary complex of a NaV C-terminal domain, a fibroblast growth factor homologous factor, and calmodulin. Structure *20*, 1167–1176.

Wen, H., and Levitan, I.B. (2002). Calmodulin is an auxiliary subunit of KCNQ2/3 potassium channels. J. Neurosci. *22*, 7991–8001.

Whicher, J.R., and MacKinnon, R. (2016). Structure of the voltage-gated K^+ channel Eag1 reveals an alternative voltage sensing mechanism. Science *353*, 664–669.

Wiener, R., Haitin, Y., Shamgar, L., Fernández-Alonso, M.C., Martos, A., Chomsky-Hecht, O., Rivas, G., Attali, B., and Hirsch, J.A. (2008). The KCNQ1 (Kv7.1) COOH terminus, a multitiered scaffold for subunit assembly and protein interaction. J. Biol. Chem. *283*, 5815–5830.

Xia, Z., and Storm, D.R. (2005). The role of calmodulin as a signal integrator for synaptic plasticity. Nat. Rev. Neurosci. *6*, 267–276.

Xu, Q., Chang, A., Tolia, A., and Minor, D.L., Jr. (2013). Structure of a Ca(2+)/CaM:Kv7.4 (KCNQ4) B-helix complex provides insight into M current modulation. J. Mol. Biol. *425*, 378–394.

Yu, Y., Ulbrich, M.H., Li, M.H., Buraei, Z., Chen, X.Z., Ong, A.C., Tong, L., Isacoff, E.Y., and Yang, J. (2009). Structural and molecular basis of the assembly of the TRPP2/PKD1 complex. Proc. Natl. Acad. Sci. USA *106*, 11558–11563.

Yu, Y., Ulbrich, M.H., Li, M.H., Dobbins, S., Zhang, W.K., Tong, L., Isacoff, E.Y., and Yang, J. (2012). Molecular mechanism of the assembly of an acid-sensing receptor ion channel complex. Nat. Commun. *3*, 1252.

Yus-Najera, E., Santana-Castro, I., and Villarroel, A. (2002). The identification and characterization of a noncontinuous calmodulin-binding site in noninactivating voltage-dependent KCNQ potassium channels. J. Biol. Chem. *277*, 28545–28553.

Zaydman, M.A., and Cui, J. (2014). PIP2 regulation of KCNQ channels: Biophysical and molecular mechanisms for lipid modulation of voltage-dependent gating. Front. Physiol. *5*, 195.

Zaydman, M.A., Silva, J.R., Delaloye, K., Li, Y., Liang, H., Larsson, H.P., Shi, J., and Cui, J. (2013). Kv7.1 ion channels require a lipid to couple voltage sensing to pore opening. Proc. Natl. Acad. Sci. USA *110*, 13180–13185.

Zhang, M., Abrams, C., Wang, L., Gizzi, A., He, L., Lin, R., Chen, Y., Loll, P.J., Pascal, J.M., and Zhang, J.F. (2012). Structural basis for calmodulin as a dynamic calcium sensor. Structure *20*, 911–923.

STAR★METHODS

KEY RESOURCES TABLE

REAGENT or RESOURCE	SOURCE	IDENTIFIER
Antibodies		
mouse monoclonal Anti-HA antibody	Sigma-Aldrich	Cat#H9658, RRID:AB_260092
rabbit monoclonal Anti-GFP antibody	Cell Signaling	Cat#2555S, RRID:AB_10692764
rabbit monoclonal Anti-tubulin antibody	Cell Signaling	Cat#2144S, RRID:AB_2210548
HRP-linked anti-mouse antibody	Cell Signaling	Cat#7074S, RRID:AB_2099233
HRP-linked anti-rabbit antibody	Cell Signaling	Cat#7076S, RRID:AB_330924
Chemicals, Peptides, and Recombinant Proteins		
2YT media	Teknova	Cat#Y0215
Isopropyl β-D-1-thiogalactopyranoside (IPTG)	OmniPur	Cat#5815
DNase I	Roche	Cat#1010415900
tris(2-carboxyethyl)phosphine (TCEP)	Soltec Ventures	Cat#M115
phenylmethylsulfonyl fluoride (PMSF)	Sigma-Aldrich	Cat#P7626
lysozyme	Sigma-Aldrich	Cat#L6876
Calcium Chloride ($CaCl_2$)	EMD	Cat#10035-04-8
ethylene glycol-bis(β-aminoethyl ether)-N,N,N',N'- tetraacetic acid (EGTA)	Sigma-Aldrich	Cat#E4378
Tobacco Etch Virus (TEV) protease	Van Petegem et al., 2005	N/A
lauryldimethylamine oxide (LDAO)	Anatrace	Cat#D360
Ammonium Sulfate	Fluka	Cat#9978
BisTris	EMD	Cat#2650
$Pt_2I_2(H_2NCH_2CH_2NH_2)$	Hampton	Cat#HR2-442
Magnesium Formate	Hampton	Cat#HR2-537
PEG 3350	Sigma-Aldrich	Cat#P4338
Dulbecco's modified Eagle's medium (DMEM)	GIBCO	Cat#11965-092
fetal bovine serum (FBS)	GIBCO	Cat#16140-071
L-glutamine	GIBCO	Cat#25030-081
penicillin/streptomycin	UCSF Cell Culture Facility	Cat#CCFGK004-153K01
Lipofectamine2000	Invitrogen	Cat#11668-019
Lipofectamine3000	Invitrogen	Cat#L3000001
Amphotericin B	EMD Millopore	Cat#171375
Fluo-3-AM	Sigma-Aldrich	Cat#39294
Indo-1-AM	ThermoScientific	Cat#I1203
BAPTA-AM	Abcam	Cat#ab120503
Ionomycin	Invitrogen	Cat#1874006
sulfo-NHS-SS-biotin	ThermoScientific	Cat#21331
Complete protease cocktail inhibitors	Roche	Cat#18970600
Streptavidin agarose beads	Pierce	Cat#20357
Deposited Data		
Coordinates of Apo/CaM:Kv7.4 AB domain complex	This study	PDB: 6B8L
Coordinates of Ca^{2+}/CaM:Kv7.4 AB domain 1 mM $CaCl_2$ soak	This study	PDB: 6B8M
Coordinates of Ca^{2+}/CaM:Kv7.4 AB domain 10 μM $CaCl_2$ soak	This study	PDB: 6B8N
Coordinates of Mg^{2+}/CaM:Kv7.4 AB domain	This study	PDB: 6B8P
Coordinates of Mg^{2+}/CaM:Kv7.5 AB domain	This study	PDB: 6B8Q

(*Continued on next page*)

Continued

REAGENT or RESOURCE	SOURCE	IDENTIFIER
Coordinates of Ca^{2+}/CaM:Kv7.4 B domain	Xu et al., 2013	PDB: 4GOW
Coordinates of CaM:Kv7.1 AB domain	Sachyani et al., 2014	PDB: 4UMO
Coordinates of Ca^{2+}/CaM:Kv7.3/7.2 AB domain	Strulovich et al., 2016	PDB: 5J03
Coordinates of CaM/Kv7.1	Sun and MacKinnon, 2017	PDB: 5VMS
Coordinates of Apo/CaM:Myosin V complex	Houdusse et al., 2006	PDB: 2IX7
Experimental Models: Organisms/Strains		
E.coli, Rosetta	Novagen	Cat#71401
HEK293	ATCC	Cat#CRL-1573
Recombinant DNA		
pET28HMT vector	Van Petegem et al., 2005	N/A
Kv7.4 AB (325-557, Δ 368-523)/pET28HMT	This study	N/A
Kv7.4 AD (325-645, C643A, Δ 368-492)/pET28HMT	This study	N/A
Kv7.4 BD (522-645, C643A)/pET28HMT	This study	N/A
Kv7.5 AB (361-545, Δ395-511)/pET28HMT	This study	N/A
CaM/pEGST	Van Petegem et al., 2005	N/A
Kv7.4 AD (325-645, C643A, Δ 368-492)/I346A/pET28HMT	This study	N/A
Kv7.4 AD (325-645, C643A, Δ 368-492)/I346D/pET28HMT	This study	N/A
Kv7.4 AD (325-645, C643A, Δ 368-492)/S536A/L536A/ pET28HMT	This study	N/A
Kv7.4 AD (325-645, C643A, Δ 368-492)/S536D/L540D/ pET28HMT	This study	N/A
pcDNA3.1	Invitrogen	Cat#V79020
Kv7.1/pcDNA3.1	This study	N/A
Kv7.4 (1-695)/pcDNA3.1	This study	N/A
Kv7.4 (1-645, Δ368-492)/pcDNA3.1	This study	N/A
Kv7.4 (1-645, Δ368-523)/pcDNA3.1	This study	N/A
Kv7.4 (1-645, Δ368-523)/HA tag/pcDNA3.1	This study	N/A
Kv7.4 (1-645, Δ368-523)/I346A/HA tag/pcDNA3.1	This study	N/A
Kv7.4 (1-645, Δ368-523)/I346D/HA tag/pcDNA3.1	This study	N/A
Kv7.4 (1-645, Δ368-523)/S536A/L536A/HA tag/pcDNA3.1	This study	N/A
Kv7.4 (1-645, Δ368-523)/S536D/L540D/HA tag/pcDNA3.1	This study	N/A
Kv7.5/pcDNA3.1	This study	N/A
pIRES2-eGFP	Clontech	Cat#632435
CaM/pIRES2-eGFP	This study	N/A
CaM_3(D93A)/pIRES2-eGFP	This study	N/A
CaM_4(D129A)/pIRES2-eGFP	This study	N/A
CaM_{12}(D20A/D56A)/pIRES2-eGFP	This study	N/A
CaM_{34}(D93A/D129A)/pIRES2-eGFP	This study	N/A
CaM_{1234}(D20A/D56AD93A/D129A)/pIRES2-eGFP	This study	N/A
Human $Na_V1.4$/pcDNA3.1	This study	N/A
Na_VSp1/pIRES2- eGFP	Shaya et al., 2014	N/A
Software and Algorithms		
HKL2000	Otwinowski and Minor, 1997	http://www.hkl-xray.com/
XDS	Kabsch, 2010	http://xds.mpimf-heidelberg.mpg.de/
PHENIX	Adams et al., 2010	https://www.phenix-online.org/
COOT	Emsley and Cowtan, 2004	http://www2.mrc-lmb.cam.ac.uk/personal/pemsley/coot/
MolProbity	Chen et al., 2010	http://molprobity.biochem.duke.edu/

(*Continued on next page*)

Continued

REAGENT or RESOURCE	SOURCE	IDENTIFIER
PISA	Krissinel and Henrick, 2007	http://www.ebi.ac.uk/pdbe/pisa/
MicroCal origin 7.0	OriginLab	N/A
PRIMUS	Konarev et al., 2003	https://www.embl-hamburg.de/biosaxs/
GNOM	Svergun, 1992	https://www.embl-hamburg.de/biosaxs/
SAXS MOW	Fischer et al., 2010	http://saxs.ifsc.usp.br/
ScAtter	Forster et al., 2010	http://www.esrf.eu/UsersAndScience/Experiments/CRG/BM26/SaxsWaxs/DataAnalysis/Scatter
pCLAMP 9	Molecular Devices	N/A
Clampfit 10.6	Molecular Devices	N/A
FlowJo	FlowJo, LLC.	https://www.flowjo.com/
ImageJ	Schneider et al., 2012	https://imagej.nih.gov/ij/
Other		
Poros20MC	Applied Biosystems	Cat#1542810
Amylose beads	BioLabs	Cat#E8021L
Econo-Pac 10DG column	Bio-Rad	Cat#732-2010
HiPrepQ column	GE Healthcare	Cat#29-0181-82
Superdex 75 column	Pharmacia Biotech	Cat#9723024
Superdex200 column	GE Healthcare	Cat#17-5175-01
C18 column	Vydac	Cat#218TP54

CONTACT FOR REAGENT AND RESOURCE SHARING

Further information and requests for resources and reagents should be directed to and will be fulfilled by the Lead Contact, Daniel L. Minor, Jr. (daniel.minor@ucsf.edu)

EXPERIMENTAL MODEL AND SUBJECT DETAILS

Cell Culture

Human embryonic kidney cells (HEK293) were purchased from ATCC (CRL-1573) and were grown at 37°C under 5% CO_2, in a Dulbecco's modified Eagle's medium (DMEM) supplemented with 10% fetal bovine serum (FBS), 10% L-glutamine, and antibiotics (100 IU mL^{-1} penicillin and 100 mg mL^{-1} streptomycin) (University of California, San Francisco Cell Culture Facility). The sex of cell line information is not determined.

METHOD DETAILS

Protein expression and purification

Constructs for Kv7.4 AB (residues 325-557, Δ368-523), Kv7.4 AD (residues 325-645, C643A, Δ368-492), Kv7.4 BD (residues 522-645, C643A) and Kv7.5 AB (residues 361-545, Δ395-511) were cloned into the pET28HMT vector (Novagen), which bears in series a hexahistidine tag, Maltose binding protein (MBP), and a Tobacco Etch Virus (TEV) protease site before the gene of interest (Xu et al., 2013). Each Kv7.4 and Kv7.5 construct was coexpressed with CaM, cloned into a pEGST vector (Xu et al., 2013). Proteins were expressed using Rosetta 2(DE3)pLysS Singles competent cells purchased from Novagen (71401). Following transformation, an overnight starter culture grown in 2YT was used to inoculate (10 mL/L) 6 L of 2YT media that were then grown at 37°C to an $O.D._{600nm}$ = 0.5-1.0. Thereafter, protein expression was induced with 0.4 mM of Isopropyl β-D-1-thiogalactopyranoside (IPTG) at 37°C for 4 hours. Cells were harvested by centrifugation (6000 g, 25 min), frozen in liquid nitrogen, and stored at −80°C.

Cells from each 6 L culture were resuspended in 100 mL lysis buffer (200 mM KCl, 1 mM $MgCl_2$, 10% (w/v) sucrose, DNase 25 μg mL^{-1}, 1 mM tris(2-carboxyethyl)phosphine (TCEP), 1 mM phenylmethylsulfonyl fluoride (PMSF), 20 μg mL^{-1} lysozyme, 100 mM Tris pH 8.8, and either 1 mM $CaCl_2$ to produce the Ca^{2+}/CaM form or 1 mM ethylene glycol-bis(β-aminoethyl ether)-N,N,N',N'-tetraacetic acid (EGTA) to produce the Apo/CaM form and were lysed by sonication (total 3 min using a 30 Hz cycle) on ice. Lysed cells were centrifuged at 35000 g for 40 min to remove debris. Supernant was filtered with sterile 0.45 μm Durapore PVDF membrane (Millipore) using syringe. Sample was purified using Poros20MC (Applied Biosystems) in Buffer A (250 mM KCl, 10 mM Na-HEPES, pH 7.4), after

washing unbound material with Buffer A with more than 5 column volume (CV), then eluted using a 0%–60% linear gradient of Buffer B (500 mM imidazole, 250 mM KCl, 10 mM Na-HEPES, pH 7.4) over 5 CV. The Poros20MC column elution was loaded to an amylose column (Buffer A: 250 mM KCl, 10 mM Na-HEPES, pH 7.4, Buffer B: 10 mM maltose, 250 mM KCl, 10 mM Na-HEPES, pH 7.4). Unbound material was removed by washing with Buffer A for 5 CV, then sample was eluted with Buffer B, 100% step elution with 5 CV. Protein was exchanged into to Buffer A using Econo-Pac 10DG column (Bio-Rad), and was treated with 1 mg TEV for 2 hr at RT followed by storage at 4°C overnight. The resultant reaction was applied to an amylose column and the cleaved sample was captured from the flow through, uncleaved material and MBP was eluted with amylose column Buffer B, 100% step elution with 5 CV. The buffer was exchanged to 50 mM KCl, 10 mM Tris pH 8.8 using Econo-Pac 10DG column (BioRad) and purified further by ion exchange chromatography (IEX) using a HiPrepQ column run in Buffer A (50 mM KCl, 10 mM Tris pH 8.8) and eluted using a linear gradient of Buffer B (1 M KCl, 10 mM Tris pH 8.8) over 10 column volumes. The samples were further purified by size exclusion chromatography (SEC) using either a Superdex 75 (GE Healthcare) (Kv7.4 AB and Kv7.5 AB), or Superdex200 (GE Healthcare) (Kv7.4 AD and Kv7.4 BD), run in a buffer containing 50 mM KCl, 1 mM TCEP, 10 mM Na-HEPES, pH 7.4. All of the IEX and SEC buffers also contained either 1 mM $CaCl_2$ or 1 mM EGTA to produce Ca^{2+}/CaM and Apo/CaM containing samples, respectively. Final sample quality was confirmed by SDS-PAGE.

Isothermal titration calorimetry (ITC)

For calorimetric study, the Ca^{2+}/CaM:Kv7.4 B peptide (513-560) complex was purified using the same expression and purification procedure as the Ca^{2+}/CaM:Kv7.4 AD, except the usage of Superdex 75 instead of Superdex 200. Following SEC, the Kv7.4 B peptide and CaM were separated using a preparative High Pressure Liquid Chromatography (HPLC) using a C18 column (Vydac) and a linear gradient from 40%–70% of acetonitrile, 0.1% trifluoroacetic acid over 15 column volumes. Acetonitrile and trifluoroacetic acid were removed by speed vacuum concentration and lyophilization. Lyophilized peptide was dissolved in MilliQ water and re-lyophilized. CaM N-lobe purification was done following (Van Petegem et al., 2005), except that the final SEC buffer contained 0.015% (w/v) lauryldimethylamine oxide (LDAO). Purified Kv7.4 B peptide and CaM N-lobe were dialyzed against 250 mM KCl, 0.015% (w/v) LDAO, 10 mM Na-HEPES. pH 7.4 containing either 1 mM $CaCl_2$ or 1 mM EGTA overnight at 4°C in the same dialysis chamber to ensure buffer matching. After centrifugation (30 min, 70000 g, 4°C), protein concentration was determined by absorbance at 280 nm (Edelhoch, 1967). Samples were degassed (5 min) prior to loading into a VP-ITC calorimeter (MicroCal). Titration was performed at 15°C and data were processed using MicroCal origin 7.0.

Crystallization, data collection, structure determination, and refinement

The Apo/CaM:Kv7.4 AB domain complex was concentrated using Amicon Ultra-15 centrifugal filtration device (3-kDa MW cutoff, Millipore) to 10 mg mL^{-1}. Crystals were grown by hanging drop vapor diffusion at 4°C using 1 μL of 10 mg mL^{-1} complex and 1 μL of reservoir solution (2 M ammonium sulfate, 0.1 M BisTris pH 6.5). Needle shaped crystals appeared overnight. Crystals were improved by streak seeding and grew to full size in one week. Pt soaked crystals were prepared by soaking crystals in the reservoir solution with ~0.05 mM $Pt_2I_2(H_2NCH_2CH_2NH_2)$ at 4°C overnight. Calcium and magnesium soaks were done by placing Apo/CaM:Kv7.4 AB crystals in reservoir solutions containing 10 μM or 1 mM $CaCl_2$, for 1 minute at 4°C, or 1 mM $MgCl_2$ for 30 min at 4°C. Apo/CaM:Kv7.5 AB crystals were grown by hanging drop vapor diffusion from a drop containing 1 μL of 10 mg mL^{-1} complex and 1 μL of reservoir solution (0.2 M magnesium formate, 20% PEG 3350), at 25°C. All crystals were cryoprotected with ethylene glycol, 5% step increase to 20%, and flash frozen in liquid nitrogen. For crystals containing calcium or magnesium, cryoprotection solutions contained 10 μM $CaCl_2$, 1 mM $CaCl_2$, or 1 mM $MgCl_2$ as appropriate.

Datasets were collected at 100K at ALS Beamline 8.3.1 (Berkeley) for the Apo/CaM:Kv7.4 AB domain native dataset (λ = 0.9797Å) and APS GM/CAT 23ID-B (Chicago) for the Apo/CaM:Kv7.4 AB domain Pt derivative (λ = 1.072Å) and CaM:Kv7.4 AB domain calcium and magnesium soaks, and Mg^{2+}/CaM:Kv7.5 AB domain (λ = 0.9795Å). Data were indexed and scaled using HKL2000 (Apo/CaM:Kv7.4 AB native and Pt derivative) (Otwinowski and Minor, 1997) or XDS (CaM:Kv7.4 AB domain calcium and magnesium soaks, Mg^{2+}/CaM:Kv7.5 AB domain) (Kabsch, 2010). The Apo/CaM:Kv7.4 AB domain structure was phased by SAD-MR using PHENIX (Adams et al., 2010) experimental phasing pipeline in which the Pt derivative dataset was truncated to the 5.0 Å. Following heavy atom site identification, the model was built and refined against the Apo/CaM:Kv7.4 AB domain native dataset. Structures of the 10 μM $CaCl_2$, 1 mM $CaCl_2$, and 1 mM $MgCl_2$ CaM:Kv7.4 AB domain soaks and Mg^{2+}/CaM:Kv7.5 AB domain were solved by molecular replacement using Apo/CaM:Kv7.4 AB domain as a search model in PHENIX (Adams et al., 2010). All structures were completed with alternating rounds of manual model building with COOT (Emsley and Cowtan, 2004) and refinement with PHENIX (Adams et al., 2010). Final structure quality was checked using MolProbity (Chen et al., 2010).

Small angle X-ray scattering (SAXS)

Apo/CaM:Kv7.4 AD, Ca^{2+}/CaM:Kv7.4 AD, and Ca^{2+}/CaM:Kv7.4 BD complexes were dialyzed overnight 4°C at against a buffer of 50 mM KCl, 1 mM TCEP, 5% (v/v) glycerol, 10 mM Na-HEPES pH 7.4 containing either 1 mM $CaCl_2$ or 1 mM EGTA, to produce Ca^{2+}/CaM and Apo/CaM bound states, respectively. Final sample was concentrated to 0.5 mg mL^{-1} (Amicon Ultra-15, 10-kDa MW cutoff, Millipore) and filtered right before doing SAXS experiment using Ultrafree-MC Centrifugal Filter Units, 12000 g, 1 min at 4°C. SAXS data were collected at the ALS (Berkeley) SIBYLS Beamline 12.3.1 using exposure times of 0.5 s, 1 s, 2 s, and 4 s. Intensities from the buffer data were subtracted form the sample data. Scattering curves were merged using PRIMUS (Konarev

et al., 2003). Guinier plot analysis and Radius of gyration (R_g) were evaluated using PRIMUS (Konarev et al., 2003) and using the entire scattering curve with GNOM (Svergun, 1992), separately. P(r) was analyzed using GNOM (Svergun, 1992). To determine D_{max}, P(r) was computed while constraining the function to go to zero at r_{max}, where r_{max} was varied from 100 to 200 Å. Estimated molecular weight based on the merged profile was determined using SAXS MOW (Fischer et al., 2010). Kratky plot, Porod-debye plot, and Porod debye value were calculated using Scatter (Forster et al., 2010).

Pull-down experiments

Kv7.4 AD and mutants (I346A, I346D, S536A/L536A, S536D/L540D) bearing the HMT tag were co-expressed with CaM in in *E.Coli* Rosetta, and were grown 30 mL 2YT (Kv7.4 AD and HMT tag only) or 120 mL 2YT (I346D, I346A, S536D/L540D, S536A/L540A) at 37°C to an $O.D._{600nm}$ = 0.5-1.0. Thereafter, protein expression was induced with 0.4 mM of IPTG at 37°C for 2 hours. Cells were harvested by centrifugation (6000 g, 10 min), frozen in liquid nitrogen, and stored at −80°C.

Cells were lysed using BugBuster protein extraction reagent (Millipore) for 20 min at 4°C and centrifuged at 21000 g for 50 min at 4°C. Supernants were incubated with 100 µl of amylose resin for 30 min at 4°C and purified by batch purification using three washes with 1 mL of Buffer A (250 mM KCl, 1 mM EGTA, 10 mM Na-HEPES pH 7.4) for 30 min at 4°C, followed by elution with 100 µl of Buffer B (250 mM KCl, 1mM, 10 mM maltose 1 mM EGTA, 10 mM Na-HEPES pH 7.4) incubation. The final result was analyzed by SDS-PAGE.

Electrophysiology

Kv7.1, Kv7.4 (1-695), Kv7.4 (1-645, Δ368-492), Kv7.4 (1-645, Δ368-523), and Kv7.5 were cloned into a pcDNA3.1 vector. I346A, I346D, S536A/L536A and S536D/L540D mutants have been made from Kv7.4 (1-645, Δ368-523) constructs using QuikChange Site-Directed Mutagenesis Kit (Stratagene). CaM and CaM mutants (CaM_{12}, D20A/D56A; CaM_{34}, D93A/D129A; and CaM_{1234} D20A/D56A/D93A/D129A (Keen et al., 1999)) were cloned into the first cassette of a pIRES2-eGFP vector (Clontech, Mountain View, CA, USA). The expression of GFP in the second cassette of these plasmids allowed the identification of transfected cells over-expressing the desired exogenous CaM.

HEK293 cells were co-transfected using Lipofectamine 2000 (Invitrogen, Carlsbad, CA, USA), in 35-mm diameter wells with 1 µg of DNA encoding for the Kv7.4 channel of interest and 1 µg of DNA encoding for either GFP only or CaM and GFP, which was used to identify transfected cells prior to recordings. 24h post-transfection, cells were plated onto coverslips coated with Matrigel (BD Biosciences, San Diego, CA, USA).

Whole cell potassium currents were recorded using perforated patch clamp (Horn and Marty, 1988; Rae et al., 1991) at room temperature (23 ± 2°C) 48–72 h post-transfection using a bath solution (in mM): 145 NaCl, 1 $CaCl_2$, 1 $MgCl_2$, 4 KCl, 10 HEPES (pH 7.4 adjusted NaOH) and pipette solution (in mM): 145 KCl, 5 Na_2ATP, 1 EGTA, 10 HEPES (pH 7.4 adjusted KOH), supplemented with Amphotericin B (400-600 µg/mL).

Data were sampled at 10 kHz and low-pass-filtered at 5 kHz using pCLAMP 9 (Molecular Devices, Sunnyvale, CA, USA) and an Axopatch 200B amplifier (Molecular Devices). Pipettes were pulled from borosilicate glass capillaries (TW150F-3; World Precision instruments, Sarasota, FL, USA) and polished (MF-900 microforge; Narishige, Tokyo, Japan) to obtain 2–3 MΩ resistance. Sixty to eighty percent of the voltage error due to the series resistance was compensated. Data analysis was performed using Clampfit 10.6 (Molecular Devices). Activation curves were obtained by fitting the data with the following Boltzmann equation: $I/Imax = 1/(1+\exp((V_{0.5}-Vm)/k))$, where $V_{0.5}$ is the half-activation potential, Vm is the membrane potential, and k is the slope factor. Parameters of Kv7.4 activation kinetics were determined by fitting the activation phase of the traces with a two-component exponential function $I(t) = A_1 \exp(-t/\tau_1) + A_2 \exp(-t/\tau_2) + C$, where I is the recorded current, A is the current amplitude, τ is the time constant and C is the amplitude at which the activation starts. A_1,τ_1 and A_2,τ_2 represent the parameters for the fast and slow activation components, respectively. All results are from at least two independent transfections.

Calcium level measurements by flow cytometry

Cells were transfected with Kv7.4 and CaM or CaM mutants delivered on separate pcDNA3.1 plasmids or using Kv7.4 pcDNA3.1 and pIRES2-eGFP vectors, using protocols identical to those used for electrophysiology experiments. Human $Na_V1.4$ (in pcDNA3.1) and bacterial Na_VSp1 (in pIRES2-eGFP) (Shaya et al., 2014) plasmids were used as controls. The GFP from the CaM pIRES constructs has significant spectral overlap with Fluo-3-AM. Therefore, we used two approaches to measure calcium levels, one using pcDNA3.1/Fluo-3-AM and one using pIRES/Indo-1-AM in order to cross-validate our results. 24 h post-transfection, cells were incubated in DMEM supplemented with 10% FBS, 10% L-glutamine, antibiotics (100 IU mL^{-1} penicillin and 100 mg mL^{-1} streptomycin) (University of California, San Francisco Cell Culture Facility) and 5 µM Fluo-3-AM for cells transfected with separate Kv7.4 and CaM pcDNA3.1 plasmids or 5 µM Indo-1-AM for pIRES containing cells at 37°C, for 1 h. Cells were then harvested using 0.05% trypsin, pelleted, and resuspended in ice-cold PBS containing 10 mM glucose and 10% FBS. BAPTA and Ionomycin treatments were performed with 10 µM BAPTA-AM or 10 µM Ionomycin + 1 mM $CaCl_2$. Fluorescence from 50,000 cells for each sample was measured using either a SONY SH800 FACS (Sony Biotechnology) for Fluo-3 (Excitation 488 nm, Emission 525 nm, 50 nm bandwidth) or a BD FACSAria II (BD Biosciences) for both Indo-1 (Excitation 346 nm, Emission 450nm, 50 nm bandwidth) and GFP (Excitation 488 nm, Emission 530 nm, 30 nm bandwidth). Data were analyzed with FlowJo software (FlowJo, LLC).

Biotinylation

Kv7.4 (1-645, Δ368-523) and mutants (I346A, I346D, S536A/L536A, S536D/L540D,) bearing a N-terminal HA tag were cloned to pcDNA3.1. 70% confluent HEK293 cells plated on 10 cm^2 plates were transfected with 4μg of the construct of interest and pIRES-GFP 6μg (which was used as an intracellular control) using Lipofectamine3000 (Invitrogen) and grown for two days at 37°C. For the biotinylation experiment, cells were pre-chilled with ice and all solutions were cooled with ice. Cells were washed three times with 10 mL phosphate buffered saline (PBS) (137 mM NaCl, 2.7 mM KCl, 10 mM Na_2HPO_4, 1.8 mM KH_2PO_4, pH 7.4) and then incubated for 30 min at 4°C with 3 mL PBS and 0.5 mM sulfo-NHS-SS-biotin (ThermoScientific, #21331) dissolved in MilliQ water. Cells were then washed three times with 10 mL PBS and the biotinylation reaction was quenched with 100 mM glycine and 0.5% BSA in PBS for 30 min. Cells were then washed with 10 mL PBS, 100 mM glycine three times. After final wash step, all buffers were carefully removed and cells in each plate were collected and resuspended in 1 mL lysis buffer (Na-HEPES pH7.4 30 mM, Triton X-100 1%, 1 tablet Complete protease cocktail inhibitors (Roche)). Cells were further lysed with passing through 21G needle, incubated on ice for 20 min. Debris was removed by centrifuged 20 min at 21000 g at 4°C. 100 μL supernant was kept for total cell lysate analysis, the rest (~900 μl) was incubated with gentle shaking with 75 μl of Streptavidin agarose beads (Pierce, #20357) for two hours at 4°C. Beads were washed five times with 1 mL lysis buffer. Labeled proteins were eluted with 2x Laemmli buffer with 10% β-mercaptoethanol by heating the sample at 50°C for 15 min. Lysate and eluted samples were analyzed on western blot by Western lightning ECL (PerkinElmer) reagent after incubation with mouse monoclonal anti-HA 1:2K (Sigma-Aldrich #H9658), rabbit monoclonal α-GFP 1:0.5K (Cell Signaling #2555S), and rabbit monoclonal α-tubulin 1:2K (Cell Signaling #2144S) antibodies, then secondary HRP-linked anti-mouse 1:5K (Cell Signaling #7074S, for α-HA) and HRP-linked anti-rabbit 1:2K (Cell Signaling #7076S, for anti-GFP and anti-tubulin) antibodies.

QUANTIFICATION AND STATISTICAL ANALYSIS

All the details of experiments can be found in the Method Details and figure legends. All data values are presented as mean ± SEM.

Calcium level measurements by flow cytometry

Fluorescence from 50,000 cells for each sample was measured using either a SONY SH800 FACS (Sony Biotechnology) for Fluo-3 (Excitation 488 nm, Emission 525 nm, 50 nm bandwidth) or a BD FACSAria II (BD Biosciences) for both Indo-1 (Excitation 346 nm, Emission 450nm, 50 nm bandwidth) and GFP (Excitation 488 nm, Emission 530 nm, 30 nm bandwidth). Data were analyzed with FlowJo software (FlowJo, LLC). Statistical significance was assessed by paired Student's t test. $p < 0.05$ was considered significant.

Biotinylation

For western blot quantification, band intensities of the α-HA in 'captured biotinylated fraction' and α-tubulin in 'total cell extract' were measured by ImageJ (Schneider et al., 2012) from four independent experiments. The ratio, (α-HA captured biotinylated fraction intensity/α-tubulin total cell extract intensity), was normalized by the same ration for the wild-type channel. In Figure 7D, Error bars are SEM.

DATA AND SOFTWARE AVAILABILITY

Coordinates and structure factors are deposited in the RCSB under the following ID codes. 6B8L, Apo/CaM:Kv7.4 AB domain; 6B8M, Ca^{2+}/CaM:Kv7.4 AB domain 1 mM $CaCl_2$ soak; 6B8N, Ca^{2+}/CaM:Kv7.4 AB domain 10 μM $CaCl_2$ soak; 6B8P, Mg^{2+}/CaM:Kv7.4 AB domain; 6B8Q, Mg^{2+}/CaM:Kv7.5 AB domain.

Neuron, Volume *97*

Supplemental Information

A Calmodulin C-Lobe Ca^{2+}-Dependent Switch Governs Kv7 Channel Function

Aram Chang, Fayal Abderemane-Ali, Greg L. Hura, Nathan D. Rossen, Rachel E. Gate, and Daniel L. Minor Jr.

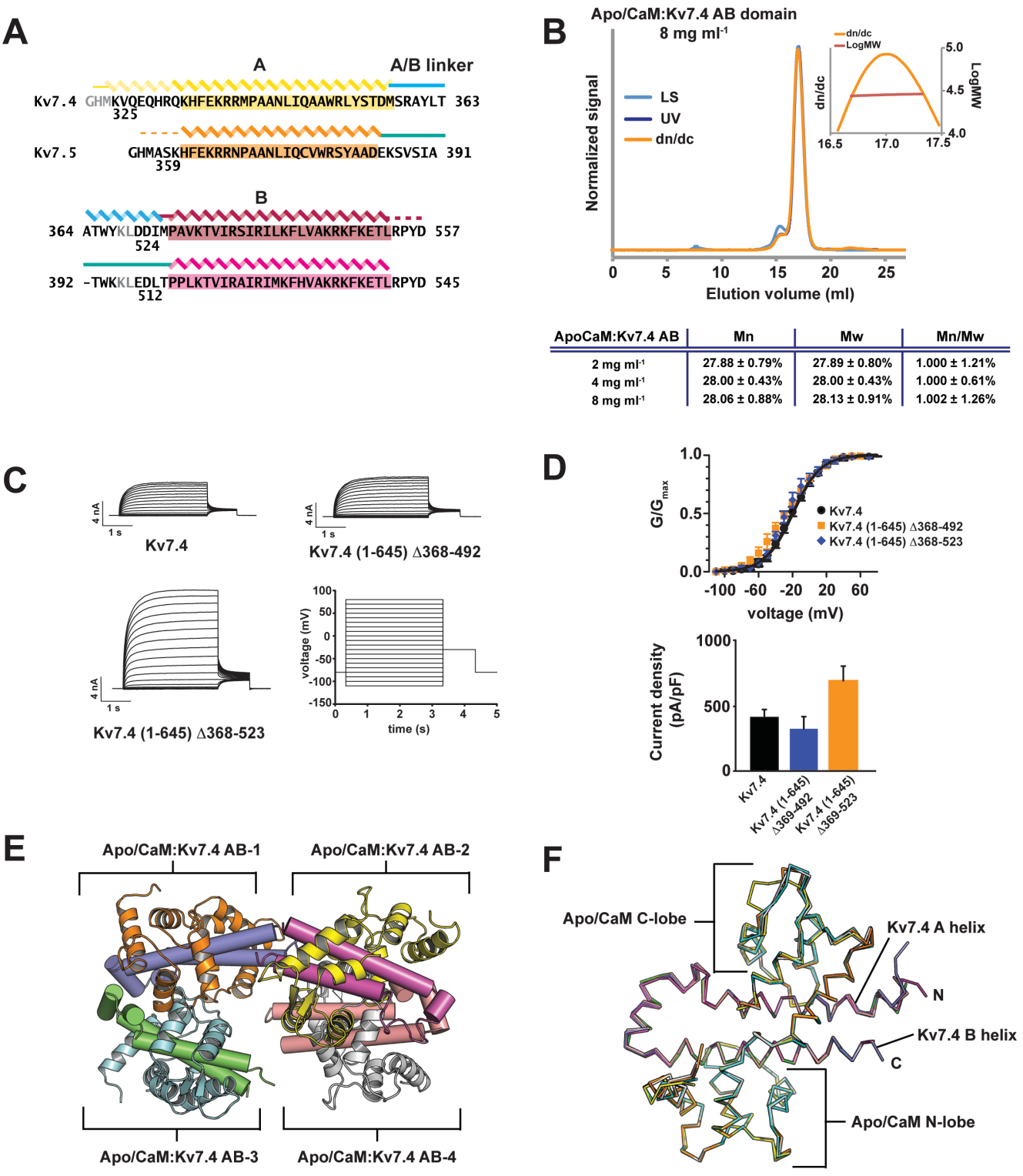

Figure S1. Crystal construct design, biochemical and functional properties, and structures of Kv7.4 and Kv7.5 AB domain constructs, Related to Figures 1 and 4, A, Diagram of AB domain crystal constructs for human Kv7.4 and Kv7.5. Grey residues 'GHM' and 'KL', derive from the expression vector and the interdomain linker, respectively. Secondary structures observed in the crystal structures are indicated. Lightly shaded portion of Kv7.4 A helix denotes residues for which

varied amounts of α-helix were observed and indicates the longest extent of helix formation. **B,** Exemplar SEC-MALS trace for the Apo/CaM:Kv7.4 AB domain complex at 8 mg ml^{-1} run in 50 mM KCl, 1 mM EGTA, 1 mM TCEP, 10 mM HEPES pH7.4. Inset shows molecular weight analysis as a function of sample concentration. Error estimates are standard deviations. **C,** Exemplar Kv7.4 potassium currents evoked using the indicated protocol. **D,** Voltage-dependent activation (upper panel) and current density at +80mV (lower panel) for the indicated Kv7.4 channels; n = 6-8. **E,** Structure of the Apo/CaM:Kv7.4 AB domain complex asymmetric unit. Individual complexes are labeled Apo/CaM:Kv7.4 AB-1 (purple and orange, chains G and H), Apo/CaM:Kv7.4 AB-2 (magenta and yellow, chains C and D), Apo/CaM:Kv7.4 AB-3 (green and cyan, chains A and B), and Apo/CaM:Kv7.4 AB-4 (salmon and grey, chains E and F). Apo/CaM is shown as ribbons and the Kv7.4 AB domain is shown as cylinders. **F,** Wire diagram showing the backbone superposition of the four Apo/CaM complexes from '**E**'.

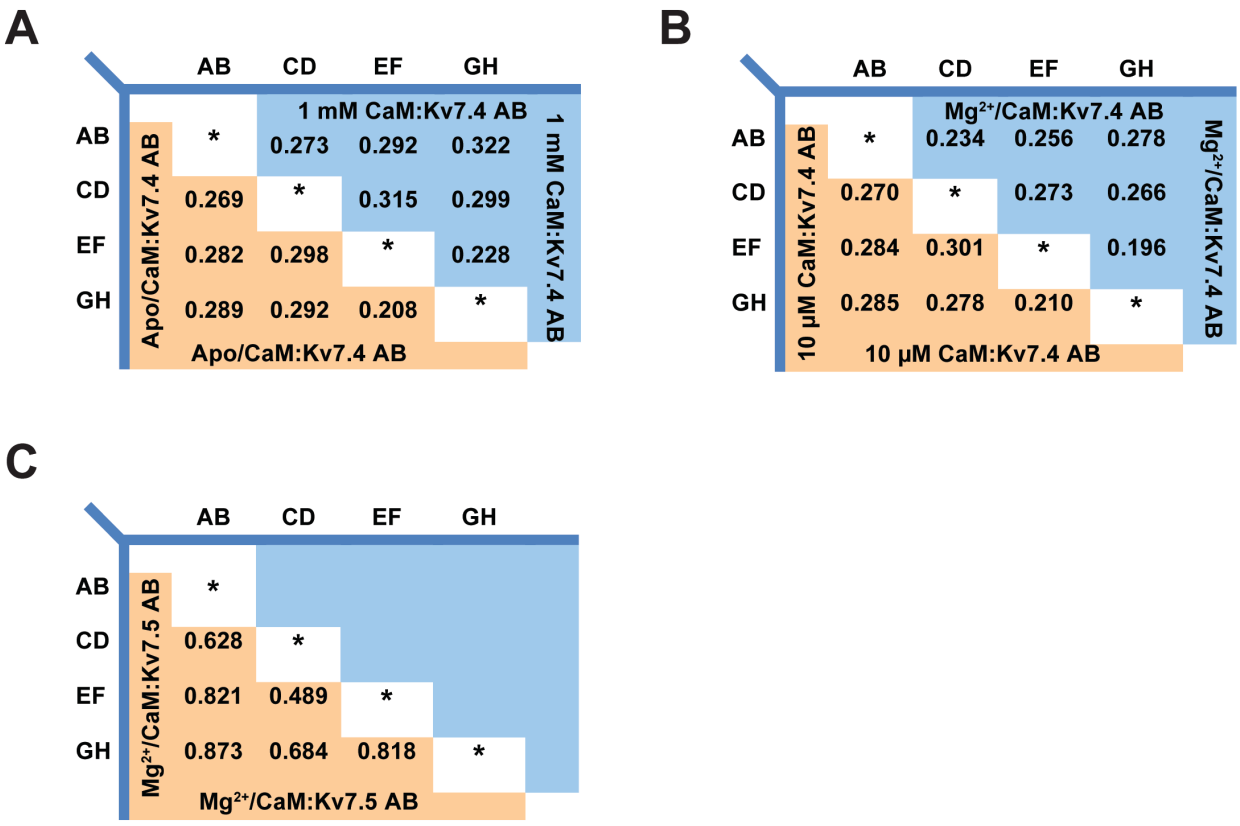

Figure S2. Comparisons of Kv7.4 and Kv7.5 AB domain structures, Related to Figures 1, 2, 3, and 4 Backbone RMSD comparisons for the indicated complexes in the asymmetric units of **A,** Apo/CaM:Kv7.4 AB (orange), 1 mM Ca^{2+} soak of Apo/CaM:Kv7.4 AB, 1 mM CaM:Kv7.4 AB (blue), **B,** 10 µM Ca^{2+} soak of Apo/CaM:Kv7.4 AB, 10 µM CaM:Kv7.4 AB (orange), 1 mM Mg^{2+} soak of Apo/CaM:Kv7.4 AB, Mg^{2+}/CaM:Kv7.4 AB (blue), and **C,** Mg^{2+}/CaM:Kv7.5 AB (orange).

Figure S3

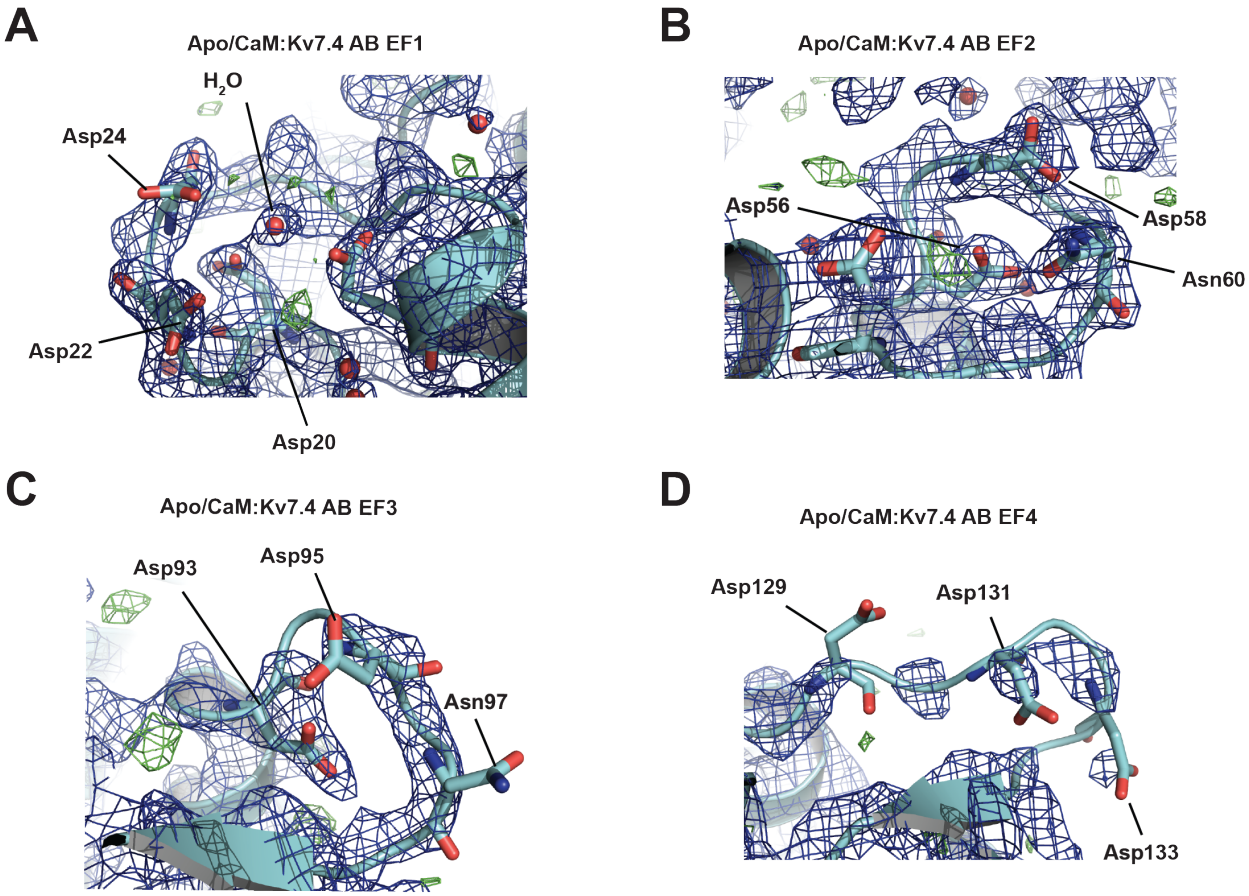

Figure S3. Exemplar electron density for Apo/CaM:Kv7.4 AB domain EF hands, Related to Figure 1, Weighted 2Fo-Fc (1.5σ), blue, and Fo-Fc (3.0σ), green, electron density for Apo/CaM:Kv7.4 AB domain EF hands **A,** EF1, **B,** EF2**, C,** EF3**,** and **D,** EF4. Model shows the final refined structure. CaM is in cyan. Nitrogen and oxygen atoms are colored blue and red, respectively. Selected CaM residues are labeled.

Figure S4

Chang *et al.*

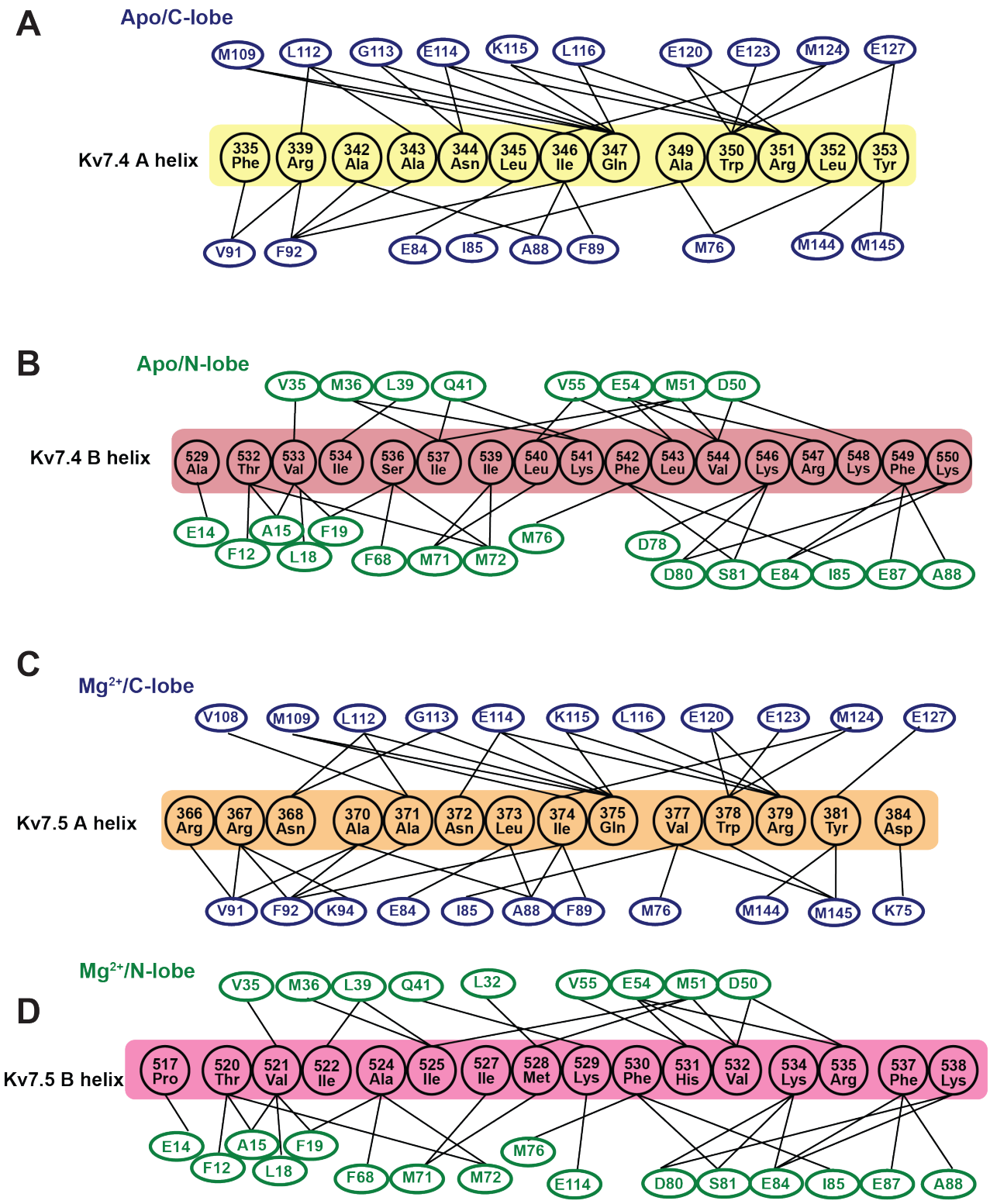

Figure S4. Interaction maps for CaM complexes with Kv7.4 and Kv7.5 AB domains, Related to Figures 1 and 4, Contacts of ≤4Å for **A,** Apo/C-lobe (blue):Kv7.4 A helix (yellow). **B,** Apo/N-lobe (green):Kv7.4 B helix (red). **C,** Mg^{2+}/C-lobe (blue):Kv7.5 A helix (orange).**D,** Mg^{2+}/N-lobe (green):Kv7.5 B helix (magenta).

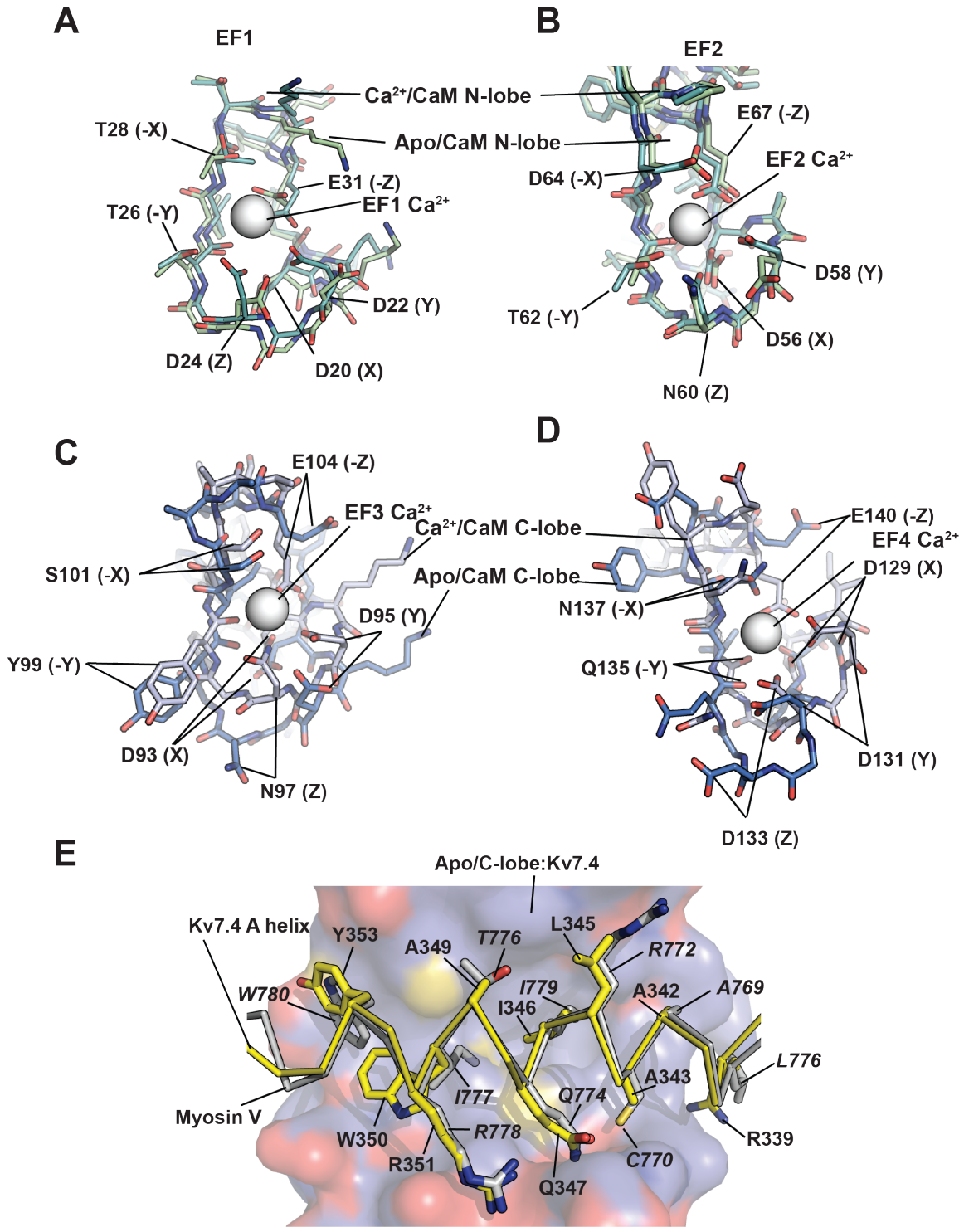

Figure S5 A-D, EF hand and C-lobe IQ domain binding comparisons, Related to Figure 2 Structure comparisons of the individual CaM EF hands from the Apo/CaM:Kv7.4 AB domain structure and the Ca^{2+}/CaM:Kv7.4 B helix structure (4GOW) (Xu et al., 2013). **A,** EF1, and **B,** EF2, Apo/CaM N-lobe (smudge), Ca^{2+}/CaM N-lobe (cyan). **C,** EF3 and **D,** EF4, Apo/CaM C-lobe and Ca^{2+}/CaM C-lobe (light blue). **E,** Structure comparison of the Apo/C-lobe interactions for the Kv7.4 A helix (yellow) and Myosin V (white) (2IX7) (Houdusse et al., 2006) with the Apo/C-lobe. Surface shows Apo/C-lobe from the Kv7.4 complex. Myosin V residues are labeled in italics.

Figure S6

Chang *et al.*

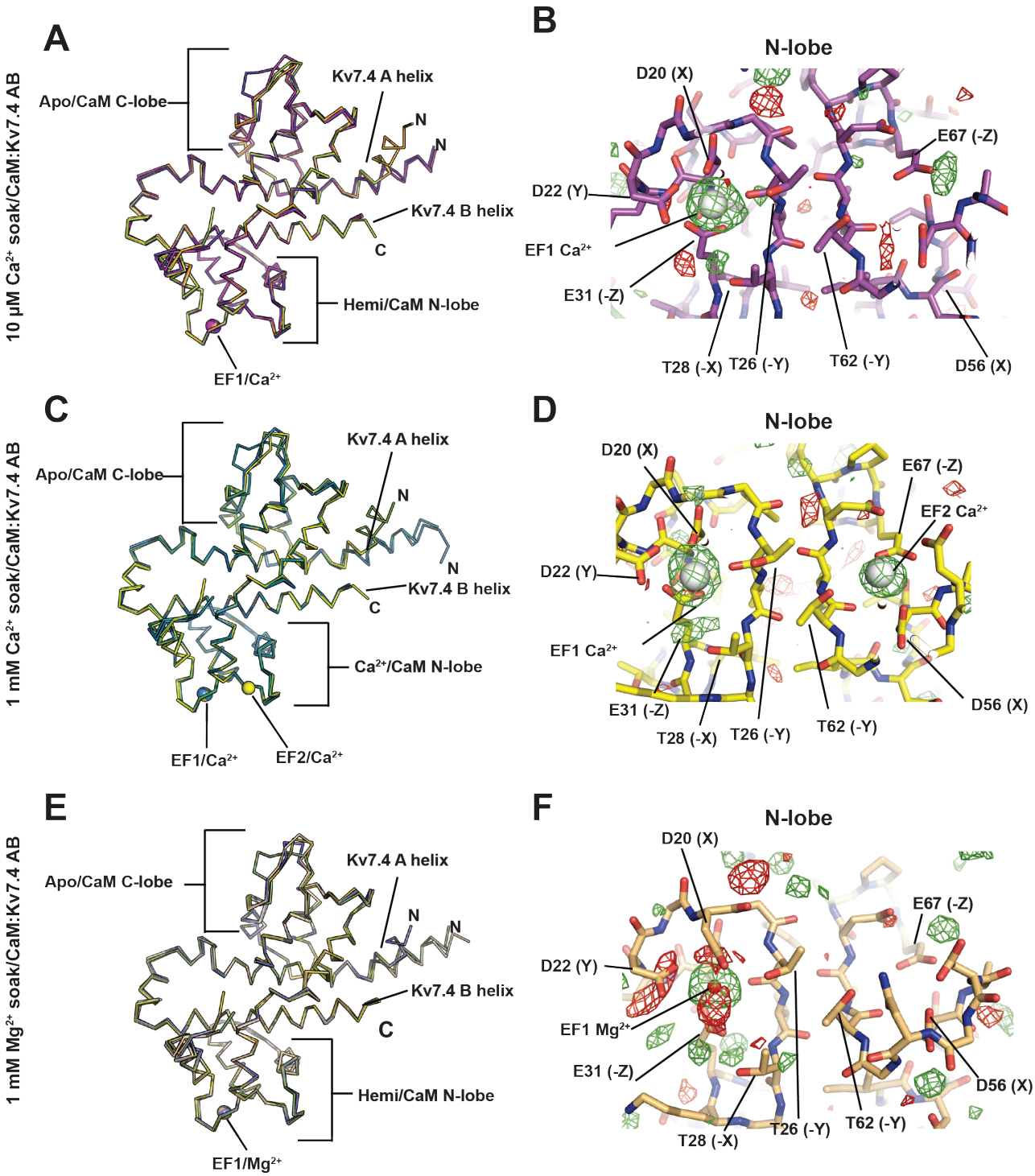

Figure S6, Structures of CaM:Kv7.4 AB complex divalent ion soaks, Related to Figure 3, A, C, and **E**, Backbone superposition wire diagrams for the four asymmetric unit copies of the CaM:Kv7.4 AB domain complexes for **A,** 10 μM Ca^{2+} soak (chains A and B, magenta; C and D, violetpurple, E and F, bright orange, and G and H, limon), **C,** 1 mM Ca^{2+} soak (chains A and B, slate; chains C and D, deepteal, chains E and F, split pea, chains G and H, yellow), and **E,** 1 mM Mg^{2+} soak (chains A and B, light orange; C and D, smudge, E and F, slate, and G and H, olive). **B, D, and F** exemplar N-lobe Fo-Fc densities (chain B) (3.0σ) for **B,** 10 μM Ca^{2+} soak, **D,** 1 mM Ca^{2+} soak, and **F,** 1 mM Mg^{2+} soak.

Figure S7

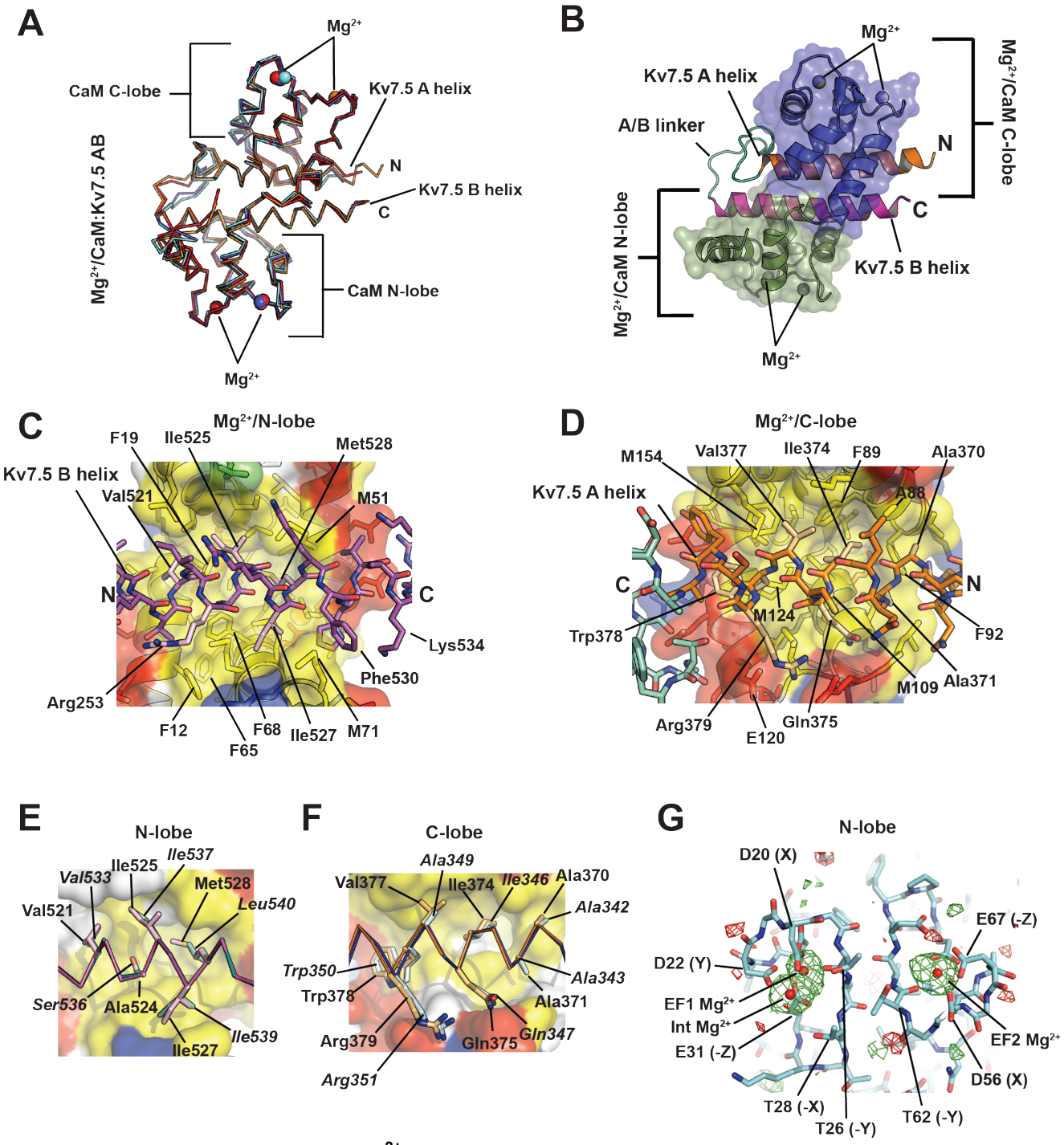

Figure S7. Structure of the Mg^{2+}/CaM:Kv7.5 AB domain complex, Related to Figure 1
A, Backbone superposition wire diagrams for the four asymmetric unit copies of the CaM:Kv7.5 AB domain complexes (chains A and B, red; chains C and D, blue, chains E and F, cyan, chains G and H, orange). **B,** Mg^{2+}/CaM:Kv7.5 AB domain complex cartoon diagram. Apo/CaM N-lobe and Apo/CaM C-lobe are shown as semitransparent surface in green and blue, respectively. Kv7.5 A helix, AB linker, and B helix region are colored orange, cyan, and magenta, respectively. Mg^{2+} ions are shown as spheres. **C,** View of the Mg^{2+}/CaM N-lobe:Kv7.5 B helix interaction. Kv7.5 B helix anchors are colored pink. **D,** View of the Mg^{2+}/CaM N-lobe:Kv7.5 A helix interaction. Kv7.5 A helix is colored orange having light orange anchor residues. Select residues are labeled using three-letter code for

Kv7.5 and single letter code for Apo/CaM. **E,** Comparison of CaM N-lobe:B helix structures of the Kv7.4 (green and pale green) and Kv7.5 (magenta and pink) complexes. **F,** CaM C-lobe:B helix structures of the Kv7.4 (dark blue and light blue) and Kv7.5 (orange and light orange) complexes. In '**C-F'** Mg^{2+}/CaM lobes are shown as semitransparent surface and stick. Hydrophobic, acidic, basic, and polar residues are colored yellow, red, blue, and green, respectively. **G,** Exemplar N-lobe Fo-Fc densities (chain B, cyan) (3.0σ) showing EF1 and EF2 bound Mg^{2+} ions. Note, all asymmetric unit complexes have a second Mg^{2+} ion, Int Mg^{2+}, coordinated at a crystal packing interface between adjacent N-lobes.

Figure S8

Chang *et al*.

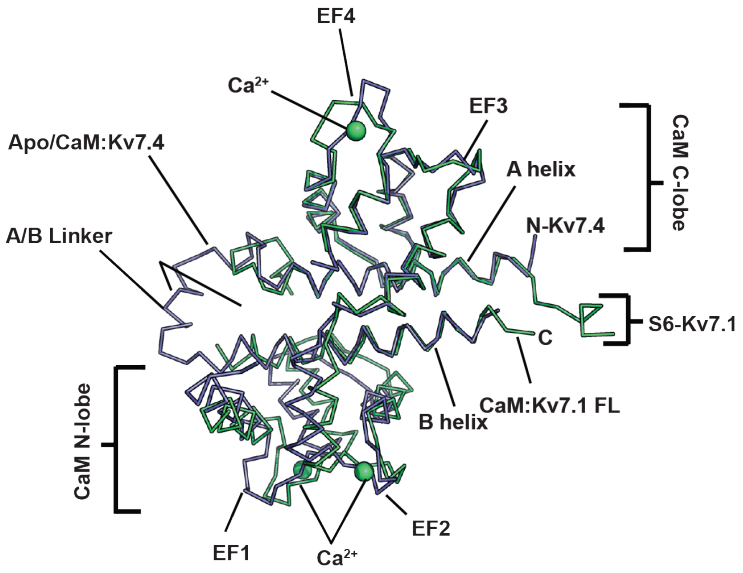

Figure S8. Comparison of Apo/CaM:Kv7.4 and CaM/Kv7.1 AB complexes, Related to Figure 4 Backbone superposition wire diagrams for Apo/CaM:Kv7.4 AB domain (chains A and B, marine), and the corresponding elements from the full length Kv7.1 complex (5VMS) (Sun and MacKinnon, 2017) lime green. EF hands and bound ions (spheres) from 5VMS are shown. Intracellular end of the Kv7.1 S6 transmembrane helix is indicated.

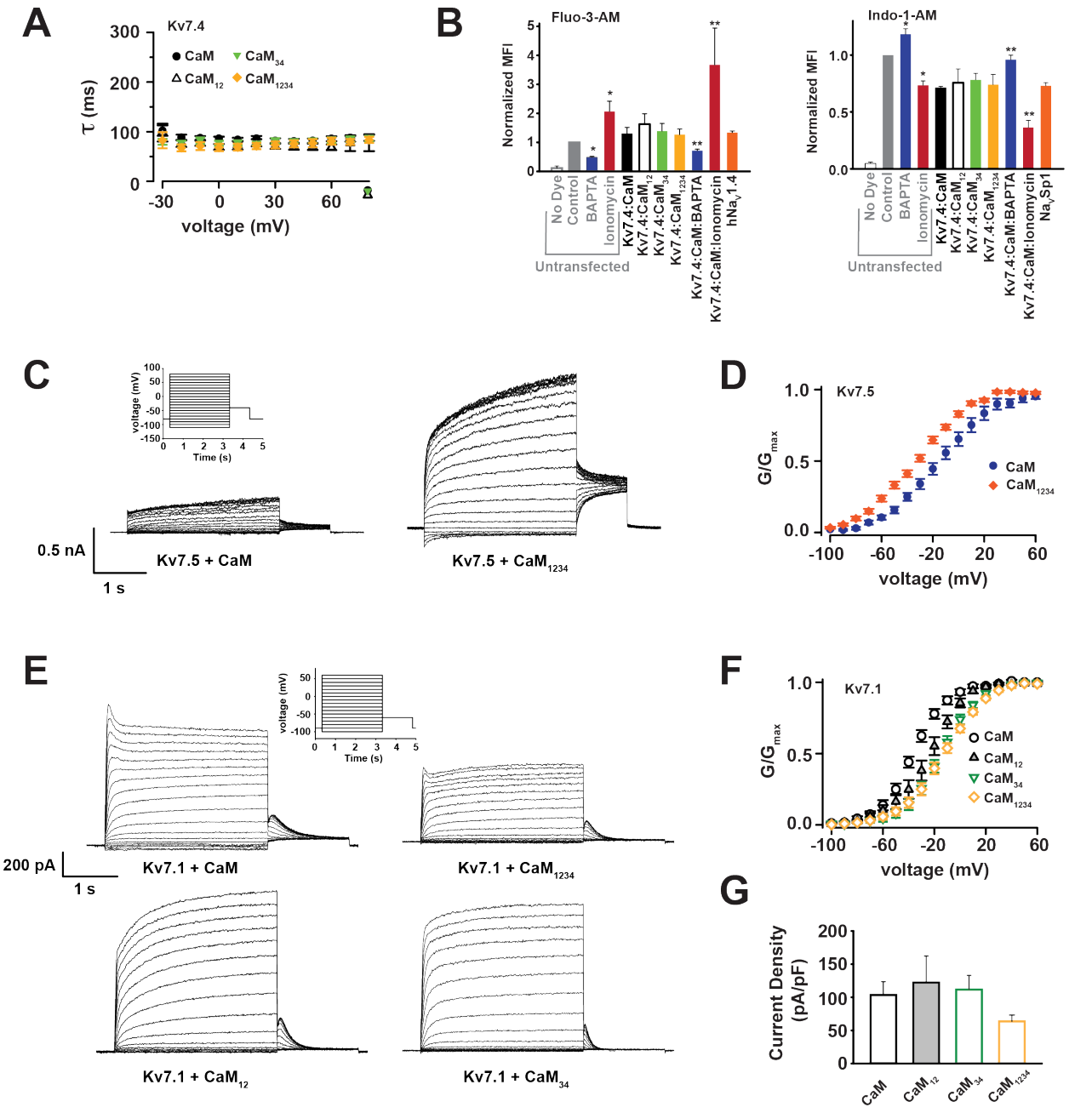

Figure S9. CaM and CaM mutant effects on Kv7 function, Related to Figure 6 A, Voltage dependence of Kv7.4 deactivation rates when co-expressed with CaM (black circles), CaM_{12} (open triangles), CaM_{34} (green inverted triangles), or CaM_{1234} (orange diamonds). **B,** Median fluorescence intensity (MFI) measured after loading the cells with Fluo-3-AM (left) or Indo-1-AM (right). Values are normalized to dye loaded untransfected cells (Control). Experiments had a measured transfection efficiency of 93.4 ± 3.0% (n=4). * $p<0.05$ relative to control; ** $p<0.05$ relative to Kv7.4:CaM. **C,** Exemplar potassium currents evoked using the indicated protocol on cells co-expressing Kv7.5 with CaM or CaM_{1234}. **D,** Voltage-dependent activation curves for Kv7.5:CaM (blue circles) and Kv7.5:CaM_{1234} (orange diamonds). **E,** Exemplar potassium currents evoked using the indicated

protocol on cells co-expressing Kv7.1 with CaM or the indicated CaM mutants. **F,** Voltage-dependent activation curves for Kv7.1:CaM combinations: CaM (open black circles), CaM_{12} (open grey triangles), CaM_{34} (inverted open green triangles), CaM_{1234} (open orange diamonds). **G,** Average current density at +60 mV from Kv7.1 co-expressed with CaM (13), CaM_{12} (14), CaM_{34} (12) or CaM_{1234} (19). n values are indicated in brackets. Values for '**D**' and '**F**' are found in Table S4. Errors are s.e.m.

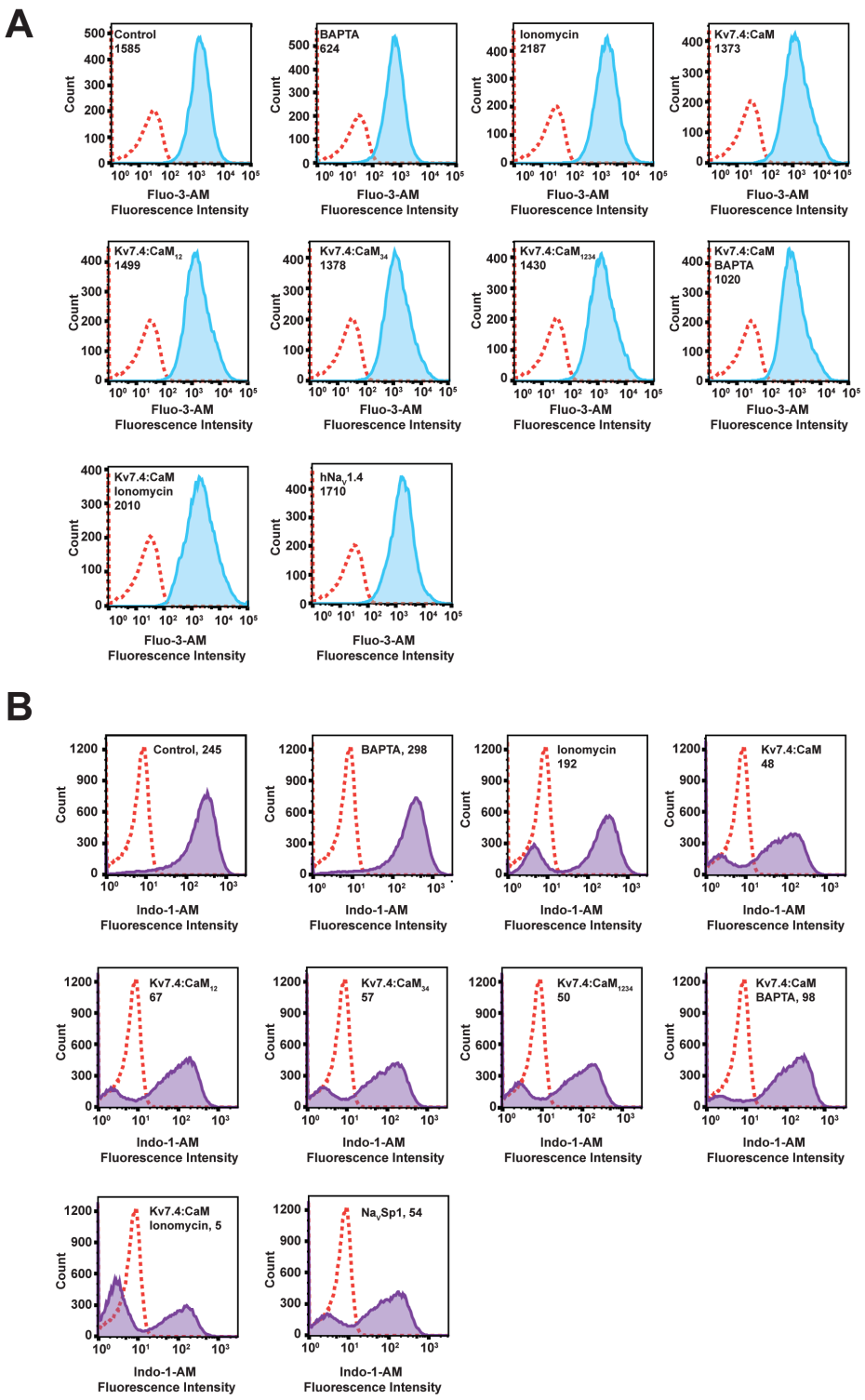

Figure S10. Co-expression of Kv7.4 with CaM and CaM mutants does not effect cytosolic Ca^{2+} concentration, Related to Figure 6 Representative flow cytometry histograms for **A,** Fluo-3-AM and **B,** Indo-1-AM measurements on untransfected cells or cells expressing the indicated channels and channel complexes. Red-dotted line indicates the profile of untransfected cells lacking the calcium indicators. Labels indicate expressed channels and complexes, cell treatment conditions, and median fluorescence intensity values.

Figure S11

Chang *et al.*

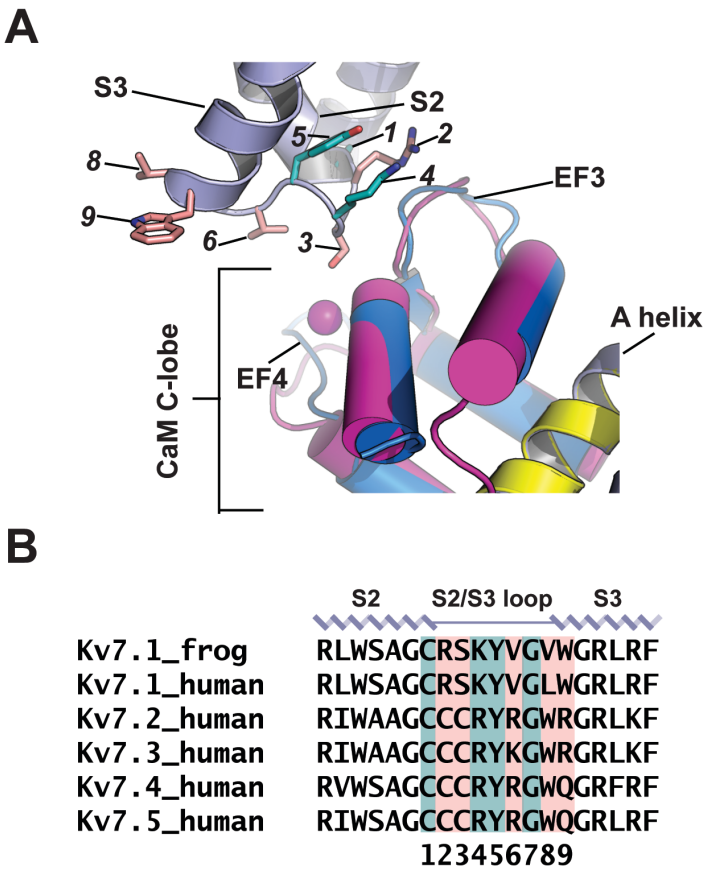

Figure S11. S2-S3 linker environment, Related to Figure 8 A, Structural comparison of CaM C-lobes from the CaM:Kv7.1 complex (5VMS)(magenta) (Sun and MacKinnon, 2017), Apo/CaM:K_V7.4: complex (marine), Residues from the S2/S3 loop of Kv7.1 are shown in stick representation, numbered 1-9, and are colored as conserved (teal) or non-conserved (salmon) between Kv7.1 and the Kv7.2-7.5 isoforms. Channel elements are labeled. S2/S3 linker positions numbers are in italics. **B,** Sequence comparison of Kv7.1 isoforms. Helical regions are indicated. S2/S3 loop positions are numbered 1-9. Sequences are: Kv7.1_frog (P70057 Kv7.1_human (P51787), Kv7.2_human (O43526), Kv7.3_human (O43525), Kv7.4_human (P56696), Kv7.5_Human (Q9NR82). Uniprot codes are in parentheses.

Table S1 Crystallographic data collection and refinement statistics

	Apo/CaM:Kv7.4 AB (**6B8L**)		Apo/CaM:Kv7.4 AB (soaks)			Mg^{2+}/CaM:Kv7.5 AB (**6B8Q**)
	Native	Pt derivative	1 mM $CaCl_2$ (**6B8M**)	10 μM $CaCl_2$(**6B8N**)	1 mM $MgCl_2$(**6B8P**)	
Data Collection						
Space group	*I*222	*I*222	*I*222	*I*222	*I*222	$P2_12_12_1$
Cell dimensions *a*/*b*/*c* (Å)	108.4/142.5/164.3	108.4/142.5/164.3	108.2/143.9/164.3	108.3/143.4/164.5	108.1/142.9/164.1	70.8/116.9/119.8
α/β/γ (°)	90.0/90.0/90.0	90.0/90.0/90.0	90.0/90.0/90.0	90.0/90.0/90.0	90.0/90.0/90.0	90.0/90.0/90.0
Resolution (Å)	50.00-2.30 (2.34-2.30)	50.00-5.00 (5.09-5.00)	15.00-2.30 (2.44-2.30)	15.00-2.20 (2.25-2.20)	15.00-2.20 (2.25-2.20)	50.00-2.60 (2.75-2.60)
R_{meas} (%)	12.8 (99.8)	8.2 (15.5)	21.5 (>100)	18.1 (>100)	10.2 (>100)	16.5 (>100)
I/σI	15.5 (4.8)	29.5 (21.6)	7.9 (0.7)	8.3 (0.7)	12.7 (1.4)	8.6 (0.8)
$CC_{1/2}$	0.982 (0.932)	0.996 (0.994)	0.996 (0.498)	0.997 (0.424)	0.999 (0.693)	0.996 (0.253)
Completeness (%)	100 (100)	100 (100)	99.6 (99.9)	99.6 (99.5)	99.6 (99.6)	99.9 (99.5)
Redundancy	7.3(7.4)	7.8 (7.8)	10.6 (10.0)	10.7 (10.6)	9.1 (9.1)	9.3 (9.7)
Unique reflections	57499 (5217)	10901 (545)	56855 (5570)	64716 (6343)	64566 (6341)	31294 (3069)
Wilson B-factor	31.8	77.2	40.8	41.7	41.8	60.5
Refinement						
R_{work} / R_{free} (%)	19.8/24.6		22.8/26.2	22.0/26.4	20.7/24.0	22.2/27.0
No. of chains in AU	8		8	8	8	8
No. of protein atoms	6951		7143	7121	7087	6608
No. of ligand atoms	25		31	24	29	15
No. of water atoms	284		223	293	296	25
RMSD bond lengths (Å)	0.007		0.003	0.002	0.002	0.003
RMSD angles (°)	0.840		0.504	0.419	0.447	0.533
Ramachandran (%)						
Favored	98.2		96.8	97.5	97.7	95.3
Allowed	1.8		3.2	2.5	2.3	4.3
Outliers	0.0		0.0	0.0	0.0	0.4

Table S1. Crystallographic data collection and refinement statistics, Related to Figures 1, 3, and 4, PDB codes are shown in bold.

$R_{meas} = \sum_{hkl}\{N(hkl)/[N(hkl)-1]\}^{1/2} \times \sum_i |I_i(hkl) - \langle I(hkl)\rangle| / \sum_{hkl}\sum_i I_i(hkl)$

Parameters for the highest resolution shell are shown in parentheses

Pt derivative was prepared using ($[Pt_2I_2(H_2NCH_2CH_2NH_2)_2](NO_3)_2$)

Table S2 Comparison of structures of CaM:Kv7 AB domain complexes

		Apo/CaM:K_V7.4 AB	Ca^{2+}/CaM:K_V7.4 AB (1 mM)	Ca^{2+}/CaM:K_V7.4 AB (10 μM)	Mg^{2+}/CaM:K_V7.4 AB	Mg^{2+}/CaM:K_V7.5 AB	CaM:K_V7.1 AB (Sachyani et al., 2014)	Ca^{2+}/CaM:K_V7.3/7.2 AB (Strulovich et al., 2016)	CaM:Kv7.1 (Sun and MacKinnon, 2017)	
						CaM only				
Apo/CaM:K_V7.4 AB	K_V7 AB + CaM		*0.242* (0.204)	*0.227* (0.196)	*0.183* (0.148)	*0.767* (0.666)	*1.618* (1.566)	*1.804* (1.605)	*1.456* (1.311)	CaM only
Ca^{2+}/CaM:K_V7.4 AB (1 mM)		*0.220* (0.175)		*0.124* (0.105)	*0.146* (0.116)	*0.766* (0.676)	*1.606* (1.531)	*1.773* (1.543)	*1.508* (1.366)	
Ca^{2+}/CaM:K_V7.4 AB (10 μM)		*0.206* (0.174)	*0.114* (0.090)		*0.129* (0.112)	*0.756* (0.679)	*1.597* (1.494)	*1.777* (1.553)	*1.475* (1.335)	
Mg^{2+}/CaM:K_V7.4 AB		*0.174* (0.141)	*0.132* (0.100)	*0.121* (0.103)		*0.736* (0.659)	*1.622* (1.529)	*1.778* (1.579)	*1.531* (1.350)	
Mg^{2+}/CaM:K_V7.5 AB		*0.688* (0.596)	*0.682* (0.608)	*0.671* (0.596)	*0.658* (0.594)		*1.644* (1.543)	*1.678* (1.567)	*1.541* (1.394)	
CaM:K_V7.1 AB (Sachyani et al., 2014)		*1.650* (1.567)	*1.635* (1.534)	*1.657* (1.513)	*1.653* (1.544)	*1.593* (1.536)		*1.507* (1.307)	*0.848* (0.793)	
Ca^{2+}/CaM:K_V7.3/7.2 AB (Strulovich et al., 2016)		*1.679* (1.490)	*1.650* (1.512)	*1.654* (1.461)	*1.665* (1.507)	*1.525* (1.409)	*1.416* (1.312)		*1.696* (1.641)	
CaM:Kv7.1 (Sun and MacKinnon, 2017)		*1.463* (1.317)	*1.481* (1.333)	*1.461* (1.326)	*1.517* (1.332)	*1.480* (1.364)	*0.833* (0.769)	*1.546* (1.460)		
						CaM: AB complex				

Table S2. Structural comparison of CaM:Kv7 AB domain complexes, Related to Figures 1, 2, 3, and 4 RMSD values are shown for all atom (italics) and Cα (parenthesis) for comparisons of CaM:Kv7 AB domain complexes (orange) and CaM only (blue).

Table S3 SAXS analysis

Construct	D_{max}	R_g	Porod Volume ($Å^3$)	Porod Value
Apo/CaM:Q4AD	135 Å	44.7Å	276125	3.5
Ca^{2+}/CaM:Q4AD	149 Å	49.5 Å	422420	2.6
Ca^{2+}/CaM:Q4BD	131 Å	45.2 Å	257954	3.5

Table S3. SAXS analysis of the indicated constructs, Related to Figure 5, D_{max}, the longest axis in the P(r) function, radius of gyration (Rg), and values from the Porod analysis are listed for the indicated constructs.

Table S4 Functional parameters of Kv7.4, Kv7.5, and Kv7.1 complexes

		Channel complex	$V_{1/2}$ (mV)	k	n
Kv7.4	Kv7.4: CaM	Kv7.4:CaM	-12.4 ± 2.2	19.6 ± 0.7	12
		Kv7.4:CaM_{12}	-22.4 ± 6.2	21.5 ± 1.8	10
		Kv7.4:CaM_{34}	-43.8 ± ;4.9	12.8 ± 0.8	12
		Kv7.4:CaM_{3}	-42.2 ± 2.9	15.4 ± 0.9	10
		Kv7.4:CaM_{4}	-34.2 ± 3.5	15.0 ± 0.6	11
		Kv7.4:CaM_{1234}	-49.2 ± 3.4	14.8 ± 0.4	8
	BAPTA	Kv7.4:CaM	-36.8 ± 3.7	14.0 ± 0.6	10
		Kv7.4:CaM_{34}	-45.2 ± 1.9	12.7 ± 1.2	8
		Kv7.4:CaM_{1234}	-39.9 ± 2.6	14.7 ± 1.0	5
	Kv7.4 Δ368-523	Kv7.4	-20.1 ± 2.4	15.9 ± 0.8	8
		Kv7.4 Δ368-492	-28.7 ± 2.8	19.4 ± 1.7	6
		Kv7.4 Δ368-523	-25.1 ± 3.1	16.1 ± 2.7	6
		Kv7.4 I346A	-19.7 ± 3.5	18.0 ± 1.4	13
		Kv7.4 I346A + CaM	-12.4 ± 4.1	16.2 ± 1.5	9
		Kv7.4 S536A/L540A	-32.5 ± 5.6	19.1 ± 2.6	7
Kv7.5		Kv7.5:CaM	-13.6 ± 4.3	19.5 ± 0.9	17
		Kv7.5:CaM_{1234}	-33.2 ± 2.1	20.4 ± 0.6	21
Kv7.1		Kv7.1:CaM	-36.4 ± 1.8	13.1 ± 1.8	9
		Kv7.1:CaM_{12}	-25.3± 4.0	12.9 ± 1.0	10
		Kv7.1:CaM_{34}	-15.4 ± 2.9	13.7 ± 1.1	10
		Kv7.1:CaM_{1234}	-13.5± 2.6	15.3 ± 1.0	18

Table S4 Functional parameters for Kv7.4, Kv7.5, and Kv7.1 CaM complexes, Related to Figures 6 and 7. Errors are s.e.m.